Diurnal variability of atmospheric cold pool events and associated air-sea interactions in the Bay of Bengal during the summer monsoon

Jofia Joseph[1], M. S. Girishkumar[1*], M. J. McPhaden[2], E. Pattabhi Ram Rao[1]

[1]Ministry of Earth Sciences (MoES), Indian National Centre for Ocean Information Services (INCOIS), Telangana, Hyderabad—500 055

[2]National Oceanic and Atmospheric Administration (NOAA), Pacific Marine Environmental Laboratory (PMEL), Seattle, Washington-98115

[*]Corresponding author: M. S. Girishkumar, Indian National Centre for Ocean Information Services (INCOIS), Hyderabad—500 055, India. Email: girish@incois.gov.in

Abstract

Atmospheric cold pools generated from convective downdrafts can significantly modulate air-sea interaction processes, though their variability is not yet documented in the Bay of Bengal (BoB). In this study, the seasonal and diurnal variability of cold pool events (defined as a drop in air temperature greater than 1°C within 30 minutes) in the BoB is examined using moored buoy measurements with 10-min temporal resolution at 8°N, 12°N, and 15°N along 90°E. The analysis shows that cold pools are plentiful and frequent during summer (May-September) and fall (October-November) compared to winter (December-February) and spring (March-April). Results also indicate a significant diurnal variability at 15°N and 12°N (but not 8°N) during summer, with more frequent and intense cold pool events in the afternoon. Cold pools lead to an intensification of turbulent heat exchange between the ocean and atmosphere, with latent heat loss (~80 Wm^{-2}) through both an increase in wind speed and reduction in air specific humidity and sensible heat loss (~40 Wm^{-2}) due primarily to air temperature drops. There is also a significant diurnal variability in these air-sea exchanges during the summer, with a twofold enhancement in *latent and sensible heat fluxes* associated with afternoon vs nighttime cold pools events. Finally, we establish the connection between the enhancement of afternoon cold pool events and southeastward propagating synoptic-scale rainfall activity on diurnal time scales from the western BoB.

1. Introduction

To improve coupled model simulations of Indian Summer Monsoon rainfall, it is important to document and understand the variability that occurs at the ocean and atmosphere interface. Air-sea interaction processes vary across a wide range of space scales and temporally from diurnal to interannual time scales in the tropics (Bhat et al. 2001; Webster et al. 2002; Sengupta et al. 2001a, 2001b; Bernie et al. 2005, Bernie et al. 2007; Seo et al. 2007; 2014; Rao and Sivakumar 2000; Shenoi et al. 2002, 2009; Praveen Kumar et al. 2012; Weller et al. 2016; Thangaprakash et al. 2016; Bhat and Fernando 2016; Cyriac et al. 2016; Girishkumar et al. 2017). Air-sea interactions at sub-daily time scales are moreover an important but relatively poorly understood component in the climate system. Considering the importance of diurnal time scale variability and its influence on seasonal to intraseasonal variations (Bernie et al. 2005; Kawai and Wada, 2007; Mujumdar et al. 2011; Seo et al. 2014), it is imperative to observe and document the variability of near-surface meteorological and oceanographic parameters at sub-daily time scales. Such efforts will help accurately represent air-sea interaction processes in climate prediction models and may eventually lead to better representation of intraseasonal and seasonal variations in coupled models being used for short, medium and extended range weather forecasts of the Indian Summer Monsoon (Bernie et al. 2005; Seo et al. 2007, 2014; Mujumdar et al. 2011; Li et al. 2013a).

The Bay of Bengal (BoB) is one of the regions where unique energetic air-sea interaction processes take place during the summer monsoon season (Thangaprakash et al. 2016; Girishkumar et al. 2017). For example, the dependence of latent heat flux (*LHF*) on wind speed during the summer monsoon is relatively small over the BoB compared to other tropical basins due to high surface humidity (Bhat and Fernando 2016; Thangaprash et al. 2016). Also, air temperature is relatively high compared to sea surface temperature (*SST*) during the summer monsoon leading to the sensible heat flux (*SHF*) into the ocean (Bhat and Fernando 2016**;** Thangaprash et al. 2016).

Moreover, because of the presence of persistent strong haloclines near the surface in the BoB due to large freshwater flux from river run-off and monsoon precipitation, the near-surface density stratification is primarily determined by salinity (Thadathil et al. 2007; Girishkumar et al. 2011). However, the coupling between the ocean and atmosphere at sub-daily time scales is not well explored in detail in the BoB due to a lack of high-temporal resolution near-surface meteorological and oceanographic data (Weller et al. 2016).

In the downdraft region of convective systems, rain-filled air falling into the unsaturated sub-cloud layer causes raindrops to evaporate. This evaporation cools the air and generates a cold unsaturated downdraft. When this cold-unsaturated downdraft reaches the surface, it spreads out horizontally leading to the formation of cold pool (Stull 2011; Zuidema et al. 2017). The presence of dense cold air in proximity to less dense surrounding air increases surface horizontal pressure gradients to spread the cold pool horizontally 10-200 km outwards as density current (Stull 2011; Zuidema et al. 2017 and references therein). Earlier studies have shown that the generation of atmospheric cold pools due to downdrafts from convective systems can significantly modulate air-sea interactions on sub-daily time scales (Gaynor and Ropelewski 1979; Johnson and Nicholls 1983; Young et al. 1992; Esbensen and McPhaden 1996; Saxen and Rutledge 1998; Chuda et al. 2008; Yokoi et al. 2014; De Szoeke et al. 2017).

Past studies in the BoB show an offshore propagation of rainfall and an afternoon rainfall peak in the central BoB (Mohamad et al., 2004; Basu, 2007; Figure 6a and 6b of Sahany et al., 2010; Figure 8 of Varikodan et al., 2012; Kilpatrick et al., 2017). Kilpatrick et al. (2017) find that the diurnal variability of rainfall in the BoB is modulated by offshore propagation of gravity waves due to diurnal heating over India. Thus, it is likely that the off-shore propagation of rainfall can modulate cold pool activity and associated air-sea interaction processes in the BoB on diurnal time scales. Motivated by these earlier studies, our purpose is to document the diurnal variability of cold pool activity in the BoB and its role in the diurnal modulation of air-sea interaction process. For this purpose, we use high temporal resolution (~10 min) near-surface meteorological and oceanographic data from the Research Moored Array for African-Asian-Australian Monsoon Analysis and Prediction (RAMA) moored buoys at 15°N, 12°N, and 8°N along 90°E (Figure 1) in the central BoB (McPhaden et al. 2009).

The paper is organized as follows. In Section 2, we describe the data sets and methodology. In Section 3, we investigate the characteristics (time of occurrence, intensity, and duration) of cold pool events in the BoB and the impact cold pools have on air-sea interaction processes. We also compare our results to those from other regions in the tropics based on earlier observational studies (Saxen and Rutledge 1998; Yokoi et al. 2014). Finally, we examine whether the diurnal variability of cold pool events reported in this study are related to synoptic conditions associated with diurnal rainfall activity in the BoB. We then summarize and discuss major results in section 4.

2. Data and Methods

We use near-surface meteorological and oceanographic data available from RAMA moorings at 15°N, 12°N, and 8°N along 90°E in the BoB (Figures 1 and 2). The RAMA buoys provide air temperature and relative humidity at a height of 3 m, wind speed and direction at a height of 4 m, and downwelling shortwave radiation and downwelling longwave radiation at a height of 3.5 m (McPhaden et al. 2009). The water temperature obtained from RAMA moorings at a depth of 1 m is considered as SST. Downwelling shortwave radiation and downwelling longwave radiation data are available at 2-min temporal resolution and all other parameters sampled at 10-min temporal resolution. Hence, downwelling shortwave and downwelling longwave radiation data are averaged to 10-min to facilitate the analysis. In this study, we adopt the convention that a positive value of heat flux indicates heat gain by the ocean from the atmosphere, and the negative value indicates heat loss from the ocean to the atmosphere. The seasons in this study are defined as summer (May-September), fall (October-November), winter (December-February), and spring (March-April).

SHF and *LHF* are estimated using mooring *SST*, air temperature (T_a), relative humidity, downwelling shortwave, and downwelling longwave radiation from the Coupled Ocean-Atmosphere Response Experiment (COARE 3.6) bulk flux algorithm (*Fairall et al.* 2003; Edson et al. 2013). The diurnal warm-layer and cool-skin temperature corrections were applied to the temperature measurements at 1 m depth for the computation of *LHF* and *SHF* (Fairall et al. 1996). The bulk formula for *SHF* and *LHF* can be written as

$$SHF = \rho C_p C_h U \Delta T \qquad (1)$$

$$LHF = \rho L C_e U \Delta q \qquad (2)$$

In this equation, ρ is the surface air density, C_p is the specific heat of moist air at constant pressure, L is the latent heat of vaporization, ΔT is the temperature difference between sea and air, Δq is the specific humidity difference between sea and air, U is wind speed and C_h and C_e are transfer coefficients for *SHF* and *LHF* respectively.

RAMA moorings at 12°N and 8°N do not have a longwave radiation sensor. Hence, Clouds and the Earth's Radiant Energy System (CERES) hourly downwelling longwave radiation data with 1°x1° spatial resolution (Wielicki et al. 1996) are used to estimate *LHF* and *SHF* at 12°N and 8°N. In this study, we use edition-4.1 of Terra/Aqua CERES surface downwelling longwave radiation data adjusted to all-sky conditions. These two data sets show very good temporal correspondence with a correlation coefficient of 0.92. The Root Mean Square Difference (RMSD) and bias (CERES-RAMA) between CERES and RAMA downwelling longwave radiation data at 15°N are 10.4 Wm^{-2} and -2.6 Wm^{-2}, respectively. These differences are generally small relative to the standard deviations of long-time series of high-resolution RAMA (~26 Wm^{-2}) and CERES (~24 Wm^{-2}) downwelling longwave radiation data.

We assessed the sensitivity of *LHF* and *SHF* estimates to the use of hourly CERES (defined as RAMA_CERES analysis) data instead of 10-min RAMA (RAMA analysis) downwelling longwave measurements at 15°N during summer. For this purpose, we interpolated hourly downwelling longwave data to 10-min temporal resolution. The standard deviation of *LHF* (46.2 Wm^{-2}) and *SHF* (10.5 Wm^{-2}) between these two analyses is negligibly small. In addition, the RMSD between these two estimates during the summer is approximately 0.5 Wm^{-2}, and 0.1 Wm^{-2} for *LHF* and *SHF*, respectively, values that are very small compared to the standard deviation these fluxes during summer. Also, the correlation between these two estimates is higher than 0.99 for both the *LHF* and *SHF*. The temporal evolution of *LHF* and *SHF* from RAMA analysis (black line) and RAMA_CERES (green line) analysis at 15°N, 90°E for the period 14-30 July 2009 are presented to show the excellent agreement between these two analyses (Figure 3). Thus, the above analysis indicates that the *LHF* and *SHF* estimation is not very sensitive to the choice of downwelling longwave radiation data from CERES and RAMA. Thus, for consistency we will use results from the RAMA_CERES analysis at 15°N, 12°N, and 8°N in the discussion that follows.

The high-resolution RAMA data have an adequate temporal resolution to characterize cold pool properties (Figure 3), so they provide a unique opportunity to document the sub-daily time scale variability of near-surface oceanographic and meteorological parameters associated with cold pools in the BoB. For example, time series of high temporal resolution of air temperature (T_a), air specific humidity (q_a), *LHF* and *SHF* obtained from RAMA mooring at 15°N, 90°E for the period 14-22 July 2009 show the existence of pronounced sub-daily variations with substantial reductions in air temperature (~ -4°C) and specific humidity (~ -3 g Kg^{-1}) resulting in a significant enhancement in *LHF* and *SHF* across the air-sea interface, particularly in the afternoon (Figure 3). These variations are the primary focus of our study. Note that *SHF* is generally directed from atmosphere to the ocean because air temperature is higher than SST except during cold pool events (Figure 3). This particular characteristic in the BoB results from entrainment of warm air from above the atmospheric to the surface layer due to strong wind shear during summer (Bhat and Fernando, 2016) and is distinct from most open-ocean conditions in the tropics.

The impact of cold pool events is apparent in multiple parameters such as air temperature and specific humidity (Figure 3). Following *Yokoi et al.* (2014), we identified cold pools when the air temperature drops by more than 1°C within 30 min. The primary advantage of this criterion is that the response of air-temperature due to the cold pool is well-differentiated from the background variability compared to other parameters such as specific humidity (Figure 3). Note that the cold pool identification criterion used in this study neglects weaker events with air temperature drop less than 1°C. The main advantage of our criterion is that it only identifies those events that can significantly influence air-sea interaction processes in the BoB. For instance, during the weak cold pool event with an air temperature drop of 0.5°C on 19 July 2009 (Figure 3b), the response of *LHF*, air specific humidity, and *SHF* cannot be differentiated from the background variations . The primary objective of this study is to understand the air-sea interaction processes associated with cold pool activity in the BoB, so we restrict ourselves to those cold pool events that can significantly modulate air-sea interactions as defined by the 1°C air temperature threshold criterion.

A schematic of a typical cold pool event is depicted in Figure 4. The cold pool duration is defined as the period between the start of the air temperature decrease (T_{intial}) and the time it reaches its minimum value (T_{final}). The difference in air temperature (ΔT_a) at T_{intial} and T_{final} is used to quantify cold pool intensity. The cold pool recovery time is defined in terms of an e-folding (1/e) recovery time ($T_{e\text{-}fold}$), such as the air temperature at T_{final} (T_{a_final}) increases by 63 % of ΔT_a (T_{a_final}+0.63ΔT_a). The responses of other parameters (e.g. ΔSHF) to the cold pool event are estimated as the difference between the T_{final} minus T_{intial} values.

In this study, cold pool events are categorized into single, double and multiple according to their frequency of occurrence. Cold pool events separated by 4 hours prior are considered as single events. If the gap between 2 events is less than 4-hours, it is considered as a double event; if more than two events occur consecutively with less than four-hour gap, they are considered multiple events. Single events exhibit a distinct drop and recovery. It is not always evident that double and multiple cold pool events recover to their e-folding values due to the close temporal proximity of these events.

The availability of air temperature data at each mooring location in the BoB (Figure 2) indicates that air temperature is available during October 2008 to December 2011 and December 2012 to May 2016 at 15°N; November 2009 to August 2011 and September 2012 to March 2016 at 12°N; and December 2006 to March 2010, October 2010 to May 2012, and March 2016 to December 2016 at 8°N (Figure 2). We present the statistics of cold pool, such as number, intensity, and recovery time, based on these air-temperature data.

LHF and *SHF* are available less often than air temperature because they depend on the simultaneous availability of multiple data sets (Figure 2). For example, at 15°N the *LHF and SHF* data are not available from November 2009 to October 2010 and August-October 2013 due to the lack of SST and wind data. Similarly, net surface heat flux data is not available during October 2013 at 12°N and during May-September 2007, May 2009 to March 2010, and March-December 2016 at 8°N. However, during summer (May-September), which is the primary season we focus on in this study, *LHF* and *SHF* data available for four (2009, 2013, 2014 and 2015), six (2010, 2011, 2012, 2013, 2014 and 2015) and two (2008 and 2011) years at 15°N, 12°N, and 8°N, respectively (Figure 2).

In this study, all the data are presented in Local Sidereal Time (LST; 5 hr 30 min ahead of UTC). The daily anomaly of a parameter is computed by removing the daily average from the respective day (defined as 24 hours from 0600 LST). Following Cronin and McPhaden (1999) and Clayson and Weitlich (2007) the diurnal amplitude of a parameter is defined as the difference between the maximum and minimum value in a day. For ease of interpretation, the composite evolution of meteorological parameters due to cold pool events is presented in the study. The standard error of mean for each variable is estimated through bootstrap methods (Thomson and Emery, 2014). The main advantage of these methods is that they do not require assumptions about the data distribution and they can be applied to small data samples to estimate uncertainties (Thomson and Emery 2014).

Three hourly precipitation data from the Tropical Rainfall Measuring Mission (TRMM) Multi-Satellite Precipitation Analysis (TMPA) are utilized to analyze the spatiotemporal evolution of large scale synoptic conditions associated with the diurnal variability of cold pool activity in the BoB (Huffman et al. 2007). In this study, we use version-7 of TMPA 3B42 dataset, also known as

TRMM 3B42 V7, which uses an improved algorithm over the earlier version-6. The TMPA 3B42 algorithm combines precipitation estimates from microwave sensors onboard low-earth orbiting satellites and infrared sensors onboard geostationary satellites and also uses available rain gauge data over the land to produce precipitation rate. The TRMM3B42 V7 precipitation data with 0.25°x0.25° spatial resolution is available between in the latitude band 50°S to 50°N. The 3-hourly averaged TRMM3B42 V7 rain rate values are centered at the middle of each 3-hour period. The one hourly TRMM 3G68 precipitation data is another product useful for investigating the diurnal variation of rainfall; however, its spatial resolution is coarser (0.5°x0.5°) compared to TRMM3B42 data. For the sake of brevity, we define TRMM3B42 V7 as TRMM in the rest of the paper.

3. Results

3.1. Seasonality of cold pool events

The monthly evolution of the average number of cold pool events and the percentage of days they occur at each mooring location in the BoB (Figure 5) indicates a significant seasonality at 15°N and 12°N. Relatively low values prevail at the beginning of the year followed by a sudden enhancement in the activity during May, reaching peak intensity during June-August and falling off from October onwards. The monthly average of cold pool events is low (< 7) and relatively infrequent (~16 % of days) during winter (December-February) and spring (March-April) at 15°N and 12°N (Figure 5). Conversely, the cold pool events are plentiful during summer (May-September) and fall (October-November), with monthly average of cold pool events being ~25 during summer and 20-25 during fall at 15°N and 12°N. Cold pool events were also reported on approximately 60 % of the days during summer and 40-50 % days during fall (October-November) at 15°N and 12°N (Figure 5b).

The seasonal variability of the cold pool event is relatively weak at 8°N, but there is an apparent semi-annual cycle with peak intensity during April-May and October-December at 8°N (Figure 5). The semiannual cycle may be associated with the position of intertropical convergence zone in the southern BoB and its seasonal northward and southward migration (Figure 1). Tropical cyclones in the BoB also show a bi-model structure, occurring more frequently in April–June and October–December (Girishkumar and Ravichandran, 2012; Li et al. 2013b), so that the existence of semi-annual variability in cold pool event may partially be associated with this seasonality of tropical cyclones.

During the summer, cold pool events are fewer at 8°N compared to the northern mooring locations, likely related to the seasonal distribution of rainfall during the summer in the BoB, which decreases towards the south (Figure 1a). Conversely, the cold pool events are relatively more frequent at 8°N during the fall (October-November) compared to 12°N and 15°N associated with a southward rainfall shift in the BoB (Figure 1b).

In summary, cold pool events are plentiful and frequent during the summer (May-September) and fall (October-November) compared to other seasons in the BoB, particularly, at 15°N and 12°N. Thus, we will not consider winter (December-February) and spring (March-May) in the subsequent analysis, since the relatively small number of cold pool events during these seasons may not contribute significantly to air-sea interaction processes in the BoB. In the next section, we examine the diurnal variability of cold pool events during summer (May-September) and fall (October-December).

3.2. Diurnal variability of cold pool events

The diurnal cycle of cold pool events during summer at each mooring shows a sudden enhancement in activity at 1000 LST, reaching peak intensity between 1200-1800 LST and falling off between 1800 LST-2400 LST at 15°N and 12°N (Figure 6a). The afternoon peak in the cold pool activity during summer is also evident in the Figure 3a. However, an afternoon peak in cold pool events is not evident at 8°N during the summer (Figure 6a). In contrast, there is no evidence of diurnal variability of cold pool events in the BoB during fall (October-November); instead, cold pool events are distributed roughly equally in each two-hour bin (Figure 6b).

The frequency distribution of the cold pool events in different six-hour bins (0000-0600 LST, 0600-1200 LST, 1200-1800 LST, and 1800-2400 LST) during summer (Table 2) indicates that cold pool activity has a well-defined afternoon peak between 1200-1800 LST, with 38 % of all events at 15°N and 34% of all events at 12°N occurring during this time. The presence of a well-defined afternoon peak (1200-1800 LST) in cold pool activity is evident in both single and double events at 15°N and 12°N (Table 2). However, such an afternoon peak is not evident at 8°N and cold pool events are distributed almost equally in each six-hour bin (Table 2).

Of all the cold pool events identified during the summer (May-September) and fall (October-November), 66-73 % events were single events, 18-21 % events were double events, and 9-13 % events were multiple events (Table 1). Moreover, these percentages are roughly the same at all the mooring locations (Table 1). Hence, for the sake of brevity in subsequent analyses, our discussion will focus on single events unless stated otherwise. Moreover, given the relatively small number of multiple and double cold pool events, it is difficult to form composites of these events separately with any degree of statistical reliability. Also, since cold pool activity shows a well-defined diurnal variation, we focus only on summer in the subsequent sections.

3.3. Diurnal variability of cold pool intensity

The composite evolution of air temperature four hours before and after single cold pool events for the six-hour bins (0000-0600 LST, 0600-1200 LST, 1200-1800 LST, and 1800-2400 LST) is shown in Figure 7a. The air-temperature (T_a) during a cold pool event shows a sudden reduction in half an hour and recovers gradually (Figure 7a). The percentage of occurrence of different magnitudes of the air temperature drop (ΔT_a) during cold pool events shows that the bulk (~55-65%) of the reduction ranges from -1°C to -2 °C (Figure 8a-8c). Note that at 15°N and 12°N, approximately 45% of cold pool events have ΔT_a magnitude of more than -2°C (Figure 8a and 8b). The ΔT_a associated with individual cold pool events reaches as high as -5°C with an average drop around -2°C (Figures 8a-8c).

The frequency of cold pool recovery times (e-folding recovery time of air temperature) shows that around 26 % (at 15°N and 12°N) and 34 % (at 8°N) of cold pool events recover within 30 min and a roughly similar percentage of events recover within 1 hr (Figure 8d-8f). Note also that at 15°N and 12°N, approximately 50 % of cold pool events has recovery time more than 1 hr (Figure 8d-8e). The e-folding recovery time of the individual cold pool events reaches as high as 4 hrs (~3 % events), with an average recovery time around 1 hrs 20 min (Figure 8d-8f).

The existence of diurnal variability of cold pool intensity at the mooring locations is evaluated through a composite evolution of ΔT_a (Figure 9a). The ΔT_a associated with the cold pool event shows a clear diurnal cycle at 15°N and 12°N (Figure 9a). At 15°N and 12°N, the ΔT_a values progressively increase from 0800-1000 LST and reach maximum value (-2.5 °C) around 1400-1600 LST. They then decrease afterwards, reaching a minimum value (-1.9 °C) around 0400 LST

(Figure 9a). However, an afternoon peak in the cold pool intensity is not evident at 8°N in that ΔT_a does not show any diurnal variability (Figure 9a). Note also that the e-folding recovery time of the cold pool does not show any diurnal variability (Figure not shown). In summary, the cold pool events are more frequent and intense in the afternoon during summer at 15°N and 12°N (Figure 9a).

3.4. Diurnal variability of atmospheric parameters associated with cold pools

Similar to the air-temperature, composite evolution of specific humidity of air (q_a) four hours before and after single cold pool events for the six-hour bins also shows a sudden decreasing tendency in association with cold pool (Figure 7e). The percentage of occurrence of different magnitudes of the air specific humidity drop (Δq_a) during cold pool events shows that the bulk (~60-65%) of the reduction ranges from -1 gKg^{-1} to -3 gKg^{-1} (Figures 10a-10c). The average value of Δq_a is around -1.8 g Kg^{-1} (Figures 7e and 10a-10c) but becomes as large as -4.5 g Kg^{-1} in response to some individual cold pool events (Figures 10a-10c). Note that at 15°N and 12°N, approximately 11% of cold pool events have Δq_a magnitude of more than -3 gKg^{-1}, and approximately 5% events have magnitude of less than -0.5 gKg^{-1} (Figure 9a-9b). Like ΔT_a, the composite evolution of Δq_a also shows diurnal variability at 15°N, with Δq_a showing a maximum drop (-2 g Kg^{-1}) in the afternoon and a minimum drop (-1.3 g Kg^{-1}) in the early morning (Figure 9b). Diurnal variability in Δq_a is also observed at 12°N, though its amplitude is small compared to 15°N (Figure 9b). However, diurnal variability in Δq_a is not evident at 8°N (Figure 9b).

The evolution of wind speed during the cold pool events shows sudden enhancement with an average value is around (~2.5 m s^{-1}), though its maximum intensity is reached approximately 10-20 min before air temperature reaches its peak value (Figure 7d). The frequency distribution of wind speed enhancement (ΔWS) during cold pool events shows that the bulk (~60-65%) of the enhancements range from 1 ms^{-1} to 5 ms^{-1} (Figure 10d-10f). For some individual cold pool events, *ΔWS* due to cold pool reaches as high as 8-10 m s^{-1} (Figure 10d-10e). Note that, in contrast to Δq_a, approximately 20-30% of cold pool events have a weak wind speed response of < 1 ms^{-1} (Figure 10d-10f). Moreover, *ΔWS* associated with cold pool events do not show diurnal variation (Figure 9e).

A sudden enhancement in *SHF* loss from the ocean is observed during cold pool events (Figures7c). The frequency distribution of enhanced *SHF* (*ΔSHF*) during cold pool events shows that the bulk (~50 %) of the reduction ranges from -10 Wm^{-2} to -30 Wm^{-2} (Figures 10g-10i). The average value of *ΔSHF* is around -30 Wm^{-2} (Figure 10g-10h) but it becomes as large as -80 Wm^{-2} in response to some individual cold pool events (Figure 10g-10h). Note that, at 15°N and 12°N, approximately 40% of cold pool events have *ΔSHF* magnitude of more than -30 Wm^{-2} and approximately 10% events have magnitude of less than -10 Wm^{-2} (Figure 10g-10i).

In response to cold pool events, *LHF* loss from the ocean shows an enhancement of -80 Wm^{-2} (Figures 7g), with individual events reaching -240 Wm^{-2} (Figure 3e and 10j-10l). The frequency distribution of latent heat loss (*ΔLHF*) enhancement shows approximately 40% of cold pool events have *ΔLHF* magnitude of between -40 Wm^{-2} and -100 Wm^{-2}, with approximately 30% of events having a magnitude greater than -100 Wm^{-2} (Figures 10j-10l).

As expected, the composite evolution of enhanced *SHF* loss (*ΔSHF*) due to cold pool events shows a clear diurnal cycle at 15°N and 12°N with the largest value of ~-40 W m^{-2} during 1400-1600 LST and a minimum enhancement of -20 W m^{-2} during 0200-0400 LST (Figure 9c). The composite evolution of enhanced *LHF* loss (*ΔLHF*) during cold pool events also shows a clear diurnal cycle at 15°N and 12°N with a maximum enhancement of -100 Wm^{-2} during 1400-1800 LST and a minimum of -60 W m^{-2} during 0200-0600 LST (Figure 9d). These results indicate an approximate two-fold enhancement in *LHF* and *SHF* associated with cold pool events in the afternoon compared the night at 15°N and 12°N during summer. These features suggest that air-sea interaction processes are very strong during the afternoon when the BoB experiences well-defined cold pool events during summer. However, such a diurnal variability is not apparent at 8°N.

3.5. Relative contribution of wind speed, specific humidity, and air temperature to turbulent fluxes

Wind speed and sea-air temperature difference (ΔT) are the primary parameters governing the modulation of *SHF*, while wind speed and sea-air specific humidity difference (Δq) determine the modulation of *LHF* (equations 1 and 2). Note that air temperature response (T_a; 2°C) during cold pool events is much higher than SST (~0.1°C), which indicates that the reduction in air temperature (T_a) largely determines the enhancement of ΔT (Figures 7a and 7b). Similarly, the specific humidity response (q_a; ~2 gKg^{-1}) during the cold pool events is much higher than specific humidity at the sea surface ($q_{s;}$ ~0.1 gkg^{-1}), indicating that the reduction in q_a primarily determines the enhancement of Δq (Figures 7e and 7f).

The relative contribution of wind speed and q_a (T_a) on *LHF* (*SHF*) during cold pool events is examined by isolating their response from one another. For this purpose, *SHF* is determined independently by two methods: one by retaining only the enhancement of wind speed (*SHF_WS*) and other by retaining only the reduction of air temperature (SHF_T_a). Similarly, *LHF* is estimated separately by keeping only the response of wind speed (defined as *LHF_WS*) or the air-specific humidity (defined as LHF_q_a) due to cold pool events. A 24-hr running mean is applied to the wind speed and T_a (q_a) to illustrate their effects on *SHF* (*LHF*) intensification (Figures S1a, S1b and S1d).

The composite evolution of *SHF* (*LHF*) four hours before and after single cold pool events is compared with *SHF* (*LHF*) values computed from the aforesaid methods (Figure 11). Note that the sum of SHF_T_a and *SHF_WS* (LHF_q_a and *LHF_WS*) captures the bulk (90-93 %) of the actual *SHF (LHF)* variability due to the cold pool events (Figure 11; compare black and cyan lines), which gives us confidence in the validity of this approach. From this procedure we can also infer that variability in the transfer coefficients (C_h and C_e in equations 1 and 2) plays a relatively minor role in modulating *SHF* and *LHF* during cold pool events, it is consistent with Yokoi et al. (2014).

Our analysis shows that *SHF_Ta* captures the bulk (~86-90 %) of the intensification observed in the *SHF* compared to *SHF_WS* (5-10 %) during cold pool events (Figures 11a-11c). This characteristic of *SHF* variability is evident at all the mooring locations in the BoB (Figures 11a-11c). The analysis suggests the dominant role of T_a in determining the *SHF* enhancement during cold pool events.

A similar analysis on *LHF* shows a significant contribution (~60%) by LHF_q_a, though the contribution of *LHF_WS* is also notable (~40%; Figures 11d-11e). This characteristic of *LHF* variability due to the cold pool is evident at 15°N and 12°N in the BoB (Figures 11d-11e). However, at 8°N, wind speed shows a slightly higher contribution (60 %) than q_a (50 %) to determine the increased *LHF* . These characteristics suggest that the variability of *LHF* is primarily determined by q_a and wind speed in contrast to *SHF* for which wind speed was less important (Figure 11). We note that the relative contribution of wind speed and T_a to *SHF* and wind speed and q_a to *LHF* reported here is consistent with previous studies in the equatorial Indian Ocean (Yokoi et al. *2014*) and in the tropical Pacific (Saxen and Rutledge 1998).

3.6. Large scale synoptic conditions associated with cold pool event

Six-hour composites of TRMM rainfall (Figures 12a-12d) and rainfall anomaly (Figure S2a-S2b) are examined to understand the diurnal evolution of synoptic conditions responsible for the cold pool events in the BoB. A Hovmoller diagram of rainfall and rainfall anomaly averaged over a longitude band 85°E-95°E and a latitude band 12°N-15°N in the BoB are also analyzed to identify any propagation characteristics in diurnal variability of rainfall (Figures 12e, 12f, S2e and S2f). The composite of rainfall anomaly constructed here is based on all those days with single cold pool events occurred. There is a persistent occurrence of rainfall maxima in the northeastern BoB with a maximum intensity during 0000-0600 LST (Figures 12a and S2a). The RAMA moorings at 15°N and 12°N are located at the outer periphery of these rainfall maxima (Figures 12a and 12b).

As reported by earlier studies and as evident in Figures 12e and 12f, southeastward propagation of a coherent band of rainfall maxima from the western BoB on diurnal time scale is also apparent (Sahany et al. 2010*;* Varikodan et al. 2012*;* Kilpatrick et al. 2017). During 0600-1200 LST, a band of well-defined positive rainfall anomaly exists in the western BoB aligned parallel to the coast (Figure 12b and S1b) and it moves further southeastward during 1200-1800 LST (Figure 12c and S2c). During 1800-2400 LST, the intensity of the rainfall anomaly declines and moves further southeastward (Figure 12d and S2d). The RAMA moorings at 15°N and 12°N come under the influence of this southeastward propagating rainfall band between 1300 LST-1500 LST (Figures 12e, 12f, S2e and S2f). Note that the RAMA mooring at 8°N does not come under the influence of this southeastward propagating rainfall band (Figures 12a-12d, Figures S2a-S2d), which explains why the frequent and intense cold pool events at 15°N and 12°N during the afternoon are not observed at 8°N in the BoB (Figure 6a). The strong temporal correspondence between the arrival of the southeastward propagating rainfall band and occurrence of cold pool events in the afternoon is also clearly evident in the continuous-time series observations during 14-30 July 2009 at the 15°N RAMA mooring location (Figure 3a and 3b).

The phase speed estimated from the slope of the propagating rainfall features in the BoB is approximately 23 m s^{-1} (Figures 12e and S2e) and, it is consistent with gravity wave speed as reported in earlier BoB studies (Kilpatrick et al. 2017). These features suggest that the southeastward propagation of diurnally-evolving rainfall controls sub-daily variability in cold pool events and associated air-sea interaction processes in the BoB.

4. Summary and conclusion

Atmospheric cold pools generated through downdrafts from convective systems can significantly modulate air-sea interaction processes over the ocean. Earlier studies have shown the existence of an afternoon peak in the rainfall activity during the summer (May-September) in the BoB suggesting that cold pools may also be prevalent then. Motivated by these studies, we examine the diurnal variability of atmospheric cold pools in the BoB and their role in the modulation of air-sea interaction processes using moored buoy data with a 10-min temporal resolution at 8°N, 12°N, and 15°N along 90°E.

On seasonal time scales, cold pool activity at 15°N and 12°N shows a peak intensity during summer (May-September) and fall (October-November). On the other hand, cold pool events are scarce during winter (December-February) and spring (March-April) at 15°N and 12°N. Seasonal variability in cold pool events is relatively weak at 8°N, with an apparent semi-annual cycle exhibiting peak intensity during April-May and October-December at 8°N. This semiannual cycle may be associated with the position of intertropical convergence zone in the southern BoB and the semi-annual cycle in the formation of tropical cyclones in the BoB.

A well-defined diurnal variability in the cold pool activity with an afternoon peak in occurrence is noted during summer (May-September) at 15°N and 12°N. We also find diurnal variability in the intensity of cold pool events, with more intense events tending to occur during the afternoon. In addition, though cold pool events are plentiful in the fall (October-November) in the BoB, our analysis finds no diurnal variability of these events during this season.

Our analysis shows that diurnal variability in air-sea interaction processes, with an afternoon peak, in response to cold pool events in the BoB during summer (May-September). Specifically, *LHF* and *SHF* loss from the ocean is enhanced by a factor of two in association with cold pool events during the afternoon compared the night. Our analysis shows further that during cold pool events, *LHF* is modulated through the combined influence of both wind speed and Δq. In contrast, ΔT primarily determines the variation of the *SHF* during cold pool events. The relative contribution of wind speed and Δq on *LHF* and wind speed and ΔT on *SHF* reported here is consistent with similar studies in the equatorial Indian Ocean (Yokoi et al. 2014) and in the tropical Pacific (Saxen and Rutledge 1998).

Our analysis further shows that sub-daily scale variability in cold pool activity and associated air-sea interaction processes are linked to southeastward propagation of synoptic-scale rainfall activity on diurnal time scales from the western BoB. While our discussion is primarily focused on just single cold pool events, we note that the propagating pattern in rainfall is evident in composite field of rainfall anomalies based on all the cold pool events (Figure S3). During 1200

LST-1800 LST, when the BoB experiences a well-defined afternoon peak in intense cold pool events, the core of rainfall maximum covers approximately half of the basin in the meridional direction (10°N-18°N and 86°E-92°E) (Figure 12c). This suggests that the diurnal variation of cold pool activity has a significant role in modulating air-sea interaction processes in the BoB during summer.

Cronin et al. (2019) suggest that better representation of cloud formation processes can improve the simulation of radiative and turbulent heat fluxes in numerical weather prediction models. Hence, it is essential to accurately simulate the sub-daily cold pool variability due to convective systems and associated air-sea interaction processes for better representation of turbulent heat flux in the BoB. Failure to represent this cold pool activity may lead to an inaccurate representation of net surface heat flux, which may generate errors in the simulation of upper ocean temperatures. For instance, the inability of coupled models to reproduce this diurnal variability in cold pool events in the BoB may lead to accumulated errors in net surface heat flux and associated ocean-atmosphere feedback mechanisms, potentially affecting the accuracy of subseasonal, seasonal and interannual time scale simulations.

Past studies have shown that cold pool events can modulate SST (Anderson, and Riser, 2014; Pei et al. 2018). However, the impact of cold pool events on SST in the BoB has not been examined to date. Detailed analysis on the diurnal variability of cold pool events and their influence on the SST will be the subject of a separate study.

Acknowledgments

The encouragement and facilities provided by the Director, INCOIS are gratefully acknowledged. RAMA data quality controlled and distributed by Global Tropical Moored Buoy

Array (GTMBA) project office of NOAA/Pacific Marine Environmental Laboratory, RAMA data are available from PMEL (https://www.pmel.noaa.gov/gtmba/pmel-theme/indian-ocean-rama). The distribution of the TRMM3B42v7 dataset is funded by NASA's Science Mission Directorate and data provided by Asia-Pacific Data Research Center, which is a part of international Pacific Research Center at the University of Hawai'i at Manoa, funded in part by the National Oceanic and Atmospheric Administration (NOAA). Data are available at http://apdrc.soest.hawaii.edu/datadoc/trmm_3b42_daily.php. TropFlux data are produced under a collaboration between Laboratoire d'Océanographie: Expérimentation et Approches Numériques (LOCEAN) from Institut Pierre Simon Laplace (IPSL, Paris, France) and National Institute of Oceanography/CSIR (NIO, Goa, India) and supported by Institut de Recherche pour le Développement (IRD, France). TropFlux relies on data provided by the ECMWF Re-Analysis interim (ERA-I) and ISCCP projects. Data are available at https://incois.gov.in/tropflux/data_access.jsp. The CERES data are available at https://ceres-tool.larc.nasa.gov/ord-tool/jsp/SYN1degEd41Selection.jsp. The Matlab code for coare3.6 is obtained from ftp://ftp1.esrl.noaa.gov/BLO/Air-Sea/bulkalg/cor3_6/. Graphics were generated using PyFerret. This is INCOIS contribution number XXX and PMEL contribution number 5090.

References

Anderson JE, and Riser SC, (2014) Near-surface variability of temperature and salinity in the near-tropical ocean: Observations from profiling floats. *J Geophys Res Oceans* 119:74. doi:10.1002/2014JC010112.

Basu BK (2007) Diurnal Variation in Precipitation over India during the Summer Monsoon Season: Observed and Model Predicted. *Mon Wea Rev,* 135, 2155–2167. https://doi.org/10.1175/MWR3355.1.

Bernie DJ, Woolnough SJ, Slingo JM, Guilyardi E (2005) Modeling Diurnal and Intraseasonal Variability of the Ocean Mixed Layer. *J Climate,* 18, 1190–1202. https://doi.org/10.1175/JCLI3319.1.

Bernie DJ, Guilyardi E, Madec G, Slingo JM, Woolnough SJ (2007) Impact of resolving the diurnal cycle in an ocean–atmosphere GCM. Part 1: a diurnally forced OGCM, *Clim. Dyn,* 29: 575. https://doi.org/10.1007/s00382-007-0249-6

Bhat GS, Gadgil S, Hareesh Kumar PV, Kalsi SR, Madhusoodanan P, Murty VSN, Prasada Rao, CV, Babu VR, Rao LV, Rao RR, Ravichandran M, Reddy KG, Rao PS, Sengupta D, Sikka DR, Swain J, Vinayachandran PN (2001) BOBMEX: The Bay of Bengal Monsoon Experiment. *Bull. Amer. Meteor. Soc.,* **82**, 2217–2244. https://doi.org/10.1175/1520-0477(2001)082<2217:BTBOBM>2.3.CO;2

Bhat GS, Fernando HJS (2016) Remotely driven anomalous sea-air heat flux over the north Indian Ocean during the summer monsoon season. *Oceanography* 29(2):232–241. https://doi.org/10.5670/oceanog.2016.55.

Chuda T, Niino H, Yoneyama K, Katsumata M, Ushiyama T, Tsukamoto O (2008) A statistical analysis of surface turbulent heat flux enhancements due to precipitating clouds observed in the tropical Western Pacific*, J. Meteorol. Soc. Jpn.,* 86, 439–457.

Clayson CA, Weitlich D (2007) Variability of Tropical Diurnal Sea Surface Temperature. *J. Clim*, 20, 334–352, https://doi.org/10.1175/JCLI3999.1

Cronin MF, Gentemann CL, Edson J, Ueki I, Bourassa M, Brown S, Clayson CA., Fairall CW, Farrar JT, Gille ST, Gulev S, Josey SA., Kato S, Katsumata M, Kent E, Krug M, Minnett PJ, Parfitt R, Pinker RT, Stackhouse PW Jr, Swart S, Tomita H, Vandemark D, Weller RA, Yoneyama K, Yu L, Zhang D (2019) Air-Sea Fluxes With a Focus on Heat and Momentum. *Front. Mar. Sci.* 6:430. doi: 10.3389/fmars.2019.00430

Cronin MF, McPhaden MJ (1999) Diurnal cycle of rainfall and surface salinity in the Western Pacific Warm Pool, *Geophys. Res. Lett.,*26(23), 3465–3468. doi:10.1029/1999GL010504

Cyriac A, Ghoshal T, and Shaileshbhai PR, (2016) Variability of sensible heat flux over the Bay of Bengal and its connection to Indian Ocean Dipole events, *Ocean Sci J* 51:97. https://doi.org/10.1007/s12601-016-0009-9.

De Szoeke SP, Skyllingstad ED, Zuidema P, Chandra AS (2017) Cold Pools and Their Influence on the Tropical Marine Boundary Layer. *J. Atmos. Sci.,* 74, 1149–1168. https://doi.org/10.1175/JAS-D-16-0264.1

Dickey TD, Manov DV, Weller RA, Siegel DA (1994) Determination of longwave heat flux at the air-sea interface using measurements from buoy platforms. *J. Atmospheric Ocean. Technol.,* 11(4):1,057–1,078. http://dx.doi.org/10.1175/ 1520-0426(1994)0112.0.CO;2

Edson JB, Jampana V., Weller RA, Bigorre SP, Plueddemann AJ, Fairall CW, Miller SD, Mahrt L., Vickers D, and Hersbach H (2013), on the exchange of momentum over the open ocean. J. Phys. Oceanogr. 43:1589:1610, https://doi.org/10.1175/JPO-D-12-0173.1.

Esbensen SK, McPhaden MJ (1996) Enhancement of tropical ocean evaporation and sensible heat flux by atmospheric mesoscale systems, *J. Clim.,* 9, 2307–2325.

Fairall CW, Bradley EF, Hare JE, Grachev AA, Edson JB (2003) Bulk Parameterization of Air-Sea Fluxes: Updates and Verification for the COARE Algorithm, *J. Clim.,* 16, 571-591, doi:http://dx.doi.org/10.1175/1520-0442(2003)016<0571:BPOASF>2.0.CO;2

Fairall CW, Bradley EF, Godfrey JS, Wick GA, Edson JB, Young GS (1996) Cool-skin and warm-layer effects on sea surface temperature, *J Geophys Res*, 101:**1**295:1308,https://doi.org/10.1029/95JC03190.

Gaynor JE, Ropelewski CF (1979) Analysis of the convectively modified GATE boundary layer using in situ and acoustic sounder data, *Mon. Weather Rev.,* 107, 985–993.

Girishkumar MS, Ravichandran M, McPhaden MJ, Rao RR (2011) Intraseasonal variability in barrier layer thickness in the south central Bay of Bengal. *J. Geophys. Res*.,, 116, C03009. https://doi.org/10.1029/2010JC006657

Girishkumar MS, Ravichandran M (2012), The influences of ENSO on tropical cyclone activity in the Bay of Bengal during October–December, *J. Geophys. Res.*, 117, C02033. doi:10.1029/2011JC007417.

Girishkumar MS, Joseph J, Thangaprakash VP, Pottapinjara V, McPhaden MJ (2017). Mixed layer temperature budget for the northward propagating summer monsoon intraseasonal oscillation (MISO) in the Central Bay of Bengal. *J. Geophys. Res*., 122, 8841–8854. https://doi.org/10.1002/2017JC013073.

Huffman GJ, Bolvin DT, Nelkin EJ, Wolff DB, Adler RF, Gu G, Hong Y, Bowman KP, Stocker EF (2007) The TRMM Multisatellite Precipitation Analysis (TMPA): Quasi-Global, Multiyear, Combined-Sensor Precipitation Estimates at Fine Scales. *J. Hydrometeor*., 8, 38–55. https://doi.org/10.1175/JHM560.1

Johnson RH, Nicholls ME (1983) A composite analysis of the boundary layer accompanying a tropical squall line, *Mon. Weather Rev.,* 124, 816–837.

Kawai Y, Wada A (2007) Diurnal sea surface temperature variation and its impact on the atmosphere and ocean: A Review, *J. Oceanogr.,* 63(5), 721–744.

Kilpatrick T, Xie S.-P, Nasuno T (2017) Diurnal convection-wind coupling in the Bay of Bengal. *J. Geophys. Res.Atmospheres,* 122, 9705–9720. https://doi.org/10.1002/2017JD027271

Li Y, Han W, Shinoda T, Wang C, Lien R.-C, Moum JN Wang J-W, (2013a) Effects of the diurnal cycle in solar radiation on the tropical Indian Ocean mixed layer variability during wintertime Madden–Julian oscillations. *J. Geophys. Res. Oceans,*118, 4945–4964. doi:10.1002/jgrc.20395.

Li Z, Yu W, Li T, Murty VSN, Tangang F (2013b) Bimodal character of cyclone climatology in the Bay of Bengal modulated by monsoon seasonal cycle. *J. Climate,* **26**, 1033–1046. https://doi.org/10.1175/JCLI-D-11-00627.1.

McPhaden M.J, Meyers G, Ando K, Masumoto Y, Murty VSN, Ravichandran M, Syamsudin, J. Vialard F, Yu L, Yu W (2009) RAMA: The Research Moored Array for African–Asian–Australian Monsoon Analysis and Prediction A new moored buoy array in the historically data-sparse Indian Ocean provides measurements to advance monsoon research and forecasting, *Bull. Am. Meteorol. Soc.*, 90, 459– 480. doi:10.1175/2008BAMS2608.1.

Mohamad IN, Hayashi T, Uyeda H, Terao T, Kikuchi K, (2004) Diurnal variations of cloud activity in Bangladesh and north of the Bay of Bengal in 2000, *Remote. Sens. Environ.*, 90, 3, 378-388, ISSN 0034-4257. https://doi.org/10.1016/j.rse.2004.01.011.

Mujumdar M, Salunke K, Rao SA, Ravichandran M, Goswami B (2011) Diurnal cycle induced amplification of sea surface temperature intraseasonal oscillations over the Bay of Bengal in summer monsoon season. *Geosci. Remote. Sens. Lett.,* IEEE 99:206–210.

Pei S, Shinoda, T, Soloviev A, Lien R-C (2018) Upper ocean response to the atmospheric cold pools associated with the Madden-Julian Oscillation. *Geophysical Research Letters*, 45, 5020– 5029. https://doi.org/10.1029/2018GL077825.

Praveen Kumar B, Vialard J, Lengaigne M, Murty VSN, McPhaden MJ (2012) TropFlux: Air-aea fluxes for the global tropical oceans - description and evaluation, *Clim.Dyn.,* 38, 1521-1543. doi:10.1007/s00382-011-1115-0.

Rao RR, Sivakumar R (2000) Seasonal variability of near-surface thermal structure and heat budget of the mixed layer of the tropical Indian Ocean from a new global ocean temperature climatology. *J. Geophys. Res.,* 105(C1):995–1,016. http://dx.doi.org/ 10.1029/1999JC900220

Sahany S, Venugopal V, Nanjundiah, RS (2010) Diurnal-scale signatures of monsoon rainfall over the Indian region from TRMM satellite observations, *J. Geophys. Res.,115*, D02103. doi:10.1029/2009JD012644

Saxen TR, Rutledge SA (1998) Surface fluxes and boundary layer recovery in TOGA COARE: Sensitivity to convective organization, *J. Atmos. Sci.,* 55, 2763–2781.

Sengupta D, Ravichandran M (2001a) Oscillations in the Bay of Bengal sea surface temperature during the 1998 summer monsoon. Geophysical Research Letters 28:2,033–2,036. http://dx.doi.org/ 10.1029/2000GL012548.

Sengupta D, Goswami BN Senan R (2001b) Coherent intraseasonal oscillations of ocean and atmosphere during the Asian summer monsoon. Geophysical Research Letters 28(21):4127–4130. http://dx.doi.org/10.1029/2001GL013587.

Seo KH, Schemm JKE, Wang W, Kumar A(2007). The boreal summer intraseasonal oscillation simulated in the NCEP Climate Forecast System: the effect of sea surface temperature, *Mon. Wea. Rev.,* 135, 1807–1827. doi: http://dx.doi.org/10.1175/MWR3369.1.

Seo H, Subramanian AC, Miller AJ,Cavanaugh, NR, (2014) Coupled Impacts of the Diurnal Cycle of Sea Surface Temperature on the Madden–Julian Oscillation. *J. Climate,* 27, 8422–8443. https://doi.org/10.1175/JCLI-D-14-00141.1

Shenoi SSC, Shankar D (2002) Differences in heat budgets of the near-surface Arabian Sea and Bay of Bengal: Implications for the summer monsoon, *J. Geophys. Res.*, 107(C6). doi:10.1029/2000JC000679, 2002.

Shenoi SSC, Nasnodkar N, Rajesh G, Joseph KJ, Suresh I Almeida AM (2009). On the diurnal ranges of Sea Surface Temperature (SST) in the north Indian Ocean, *J. Earth Syst. Sci.,*118(5), 483–496.

Stull R (2011) Meteorology for Scientists and Engineers, 3rd Edition Copyright, by Roland Stull Dept. of Earth, Ocean & Atmospheric Sciences University of British Columbia 2020-2207 Main Mall Vancouver, BC, Canada V6T 1Z4, ISBN-13: 978-0-88865-178-5.

Thomson R.E, and Emery WJ (2014). Data analysis methods in Physical Oceanography (Third Edition), Chapter 3 - Statistical methods and error handling, Editor(s): Richard E. Thomson, William J. Emery, Elsevier, 2014, P. 219-311, ISBN 9780123877826, https://doi.org/10.1016/B978-0-12-387782-6.00003-X

Thadathil P, Muraleedharan PM, Rao RR, Somayajulu YK, Reddy GV, Revichandran C (2007). Observed seasonal variability of barrier layer in the Bay of Bengal. J. Geophys. Res., 112, C02009. https://doi.org/10.1029/2006JC003651

Thangaprakash VP, Girishkumar MS, Suprit K, Suresh Kumar N, Chaudhuri D, Dinesh K, Kumar A, Shivaprasad S, Ravichandran M, Farrar JT, Sundar R, Weller RA (2016). What controls seasonal evolution of sea surface temperature in the Bay of Bengal? Mixed layer heat budget analysis using moored buoy observations along 90°E. *Oceanography* 29(2):202–213. http://dx.doi.org/10.5670/oceanog.2016.52.

Varikoden H., Preethi B, Revadekar JV (2012). Diurnal and spatial variation of Indian summer monsoon rainfall using tropical rainfall measuring mission rain rate. *Journal of Hydrology*, 475, 248–258. https://doi.org/10.1016/j.jhydrol.2012.09.056

Webster P, Bradley EF, Fairall CW, Godfrey JS, Hacker P, Houze Jr RA, Lukas R, Serra Y, Hummon JM, Lawrence TDM, Russell CA, Ryan MN, Sahami *K,* Zuidema P (2002). The JASMINE Pilot Study. *Bulletin of the American Meteorological Society*, **83**, 1603– 1630. https://doi.org/10.1175/BAMS-83-11-1603.

Weller RA, Farrar JT, Buckley J, Mathew S, Venkatesan R, SreeLekha J, Chaudhuri D, Suresh Kumar N, Praveen Kumar B (2016) Air-sea interaction in the Bay of Bengal. Oceanography, 29(2):28–37. http://dx.doi.org/10.5670/oceanog.2016.36.

Wielicki BA, Barkstrom BR, Harrison EF, Lee III RB, Smith GL, Cooper JE (1996) Clouds and the Earth's Radiant Energy System (CERES): An earth observing system experiment. *Bull Amer Meteor Soc*, 77:853-868. doi: 10.1175/1520-0477(1996)077<0853:CATERE>2.0.CO;2

Yokoi S, Katsumata M, Yoneyama K (2014) Variability in surface meteorology and air-sea fluxes due to cumulus convective systems observed during CINDY/DYNAMO, J. Geophys. Res. Atmos., 119, 2064–2078. doi:10.1002/2013JD020621.

Young GS, Ledvina DV, Fairall CW (1992) Influence of precipitating convection on the surface energy budget observed during a Tropical Ocean Global Atmosphere pilot cruise in the tropical western Pacific ocean. *J. Geophys. Res.,* 97, 9595–9603.

Zuidema P, Torri G, Muller C, Chand A (2017) A Survey of Precipiatation-induced Atmospheric cold pools over Ocean and Their Interactions with the Larger-Scale Environment, Surv. Geophys, 39:1283. https://doi.org/10.007/s10712-017-0447-x.

Figures captions

Figure 1. The seasonal average (1998-2017) of TRMM rainfall (mm day^{-1}) during (a) summer (May-September), (b) fall (October-November), (c) winter (December-February), and (d) spring (March-April) in the BoB. The RAMA mooring locations in the BoB are marked in pink circles.

Figure 2. The availability of air temperature (black) and turbulent heat fluxes (red; *LHF* and *SHF*) from the RAMA mooring at 15°N, 90°E, 12°N, 90°E and 8°N, 90°E.

Figure 3. (a) The hovmoller diagram of TRMM rainfall (mm hr^{-1}) averaged over a latitude band 13°N-17°N. The temporal evolution of (b) air temperature (°C; T_a) (c) sensible heat flux (W m^{-2}; *SHF*), (d) air specific humidity (g $Kg^{-1;}$ q_a) and (e) latent heat flux (W $m^{-2;}$ *LHF*) from RAMA mooring at 15°N, 90°E during 14-30 July 2009. The tilted black lines in the panel (a) depict the offshore propagation of rainfall band. The pink horizontal line in the panel (a) represents the RAMA mooring location at 90°E. The cold pool events at the mooring locations are highlighted in the grey transparent shading. In the panels (c) and (e) the black line represents RAMA analysis and green line represents RAMA_CERES analysis.

Figure 4. A schematic of a typical cold pool event based on air temperature drop and its e-folding recovery time. The cold pool active duration is defined as the period between when air temperature starts to decrease (T_{intial}) and when it reaches the minimum value (T_{final}). The difference in air temperature (ΔT_a) at T_{intial} and T_{final} is used to quantify cold pool intensity The cold pool recovery time is defined in terms of an e-folding (1/e) recovery time ($T_{e\text{-}fold}$), such as the air temperature at T_{final} (T_{a_final}) increases by 63 % of ΔT_a ($T_{a\_final}+0.63\Delta T_a$). The responses of other parameters (e.g. ΔSHF) to the cold pool event are estimated as the difference between T_{final} minus and T_{intial} values.

Figure 5. The monthly evolution of (a) average number of cold pool events (b) percentage of days cold pool events were reported at 15°N, 90°E, (black) 12°N, 90°E (red) and 8°N, 90°E (green) in the BoB. The seasons in this study are defined as summer (May-September), fall

(October-November), winter (December-February), and spring (March-April). Shading represents the one-standard error and it is estimated based on year-to-year deviations from the mean seasonal cycle using bootstrap method.

. Figure 6. The average number of cold pool events observed in two-hour bins at 15°N, 90°E, (black) 12°N, 90°E (red) and 8°N, 90°E (green) in the BoB during (a) summer (May-September) and (b) fall (October-November). The pink vertical shading demarcate periods used for six-hour composites (0000-0600 LST, 0600-1200 LST, 1200-1800LST and 1800-2400LST). The 2-hourly averaged values are cantered in the middle of each two hours; for instance, the number of cold pool events corresponding to 0300 LST represents the number of events between 0200 LST and 0359 LST. Note that for the calculation we considered only those years with a minimum of 70 % data availability in a season (table-S1). Shading represents the one-standard error and it is estimated based on year-to-year deviations from the mean diurnal cycle using bootstrap method.

Figure 7. Composite evolution of anomaly of meteorological parameters 4-hr before and after the single cold pool events which occurred during 0000-0600 LST (red), 0600-1200 LST (green), 1200-1800 LST (blue) and 1800-2400LST (cyan) at (left) 15°N, 90°E, (middle) 12°N, 90°E and (right) 8°N, 90°E in summer (May-September). (a) air temperature (°C; T_a) (b) difference in sea surface temperature and air temperature (°C; ΔT), (c) sensible heat flux (W m^{-2}; *SHF*) (d) wind speed (m s^{-1}), (e) air specific humidity (g Kg^{-1}; q_a), (f) difference in specific humidity between sea surface and air (g Kg^{-1}; Δq), (g) latent heat flux (W m^{-2}; *LHF*).

Figure 8. The frequency (a, b and c) of air temperature drop (°C; ΔT_a) in 0.5°C bins (e.g. -2°C ΔT_a corresponds to percentage of events with air temperature drop between -2 to -2.5°C) and (d, e and f) e-folding recovery time (hours) in 30 min bins (e.g. 1-hour corresponds to percentage of events with recovery time between 30-min to 1-hours) due to the single cold pool events at (left) 15°N, 90°E, (middle) 12°N, 90°E and (right) 8°N, 90°E during summer (May-September). The numbers in the top and bottom panels represent the mean of air temperature drop (°C) and e-folding recovery time (hours), respectively. Note that, we considered only those cold pool events with air temperature drop more than 1°C, hence, in the panels (a)-(c) the minimum drop restricted 1°C.

Figure 9. The diurnal variability of maximum response of surface meteorological parameters due to single cold pool events with respect to pre-cold pool conditions averaged over two-hour bins during summer (May-September). (a) reduction in air temperature (°C; ΔT_a), (b) reduction in specific humidity (g Kg^{-1}; Δq_a) (c) enhancement in sensible heat flux loss (W m^{-2}; ΔSHF) (d) enhancements in latent heat flux loss (W m^{-2}; ΔLHF), (e) enhancement in wind speed (m s^{-1}; ΔWS) at (left) 15°N, 90°E, (middle) 12°N, 90°E and (right) 8°N, 90°E. The 2-hourly averaged values are centered at the middle of each two-hour period; for instance, ΔT_a corresponding to 0300 LST represents the average value between 0200 LST and 0339 LST. Shading represents the one-standard error and it is estimated based on the deviations of data from the mean in each two-hour bins using bootstrap method. Time in LST hours. Note that response of surface meteorological parameters shows a sudden enhancement around 1000 LST and reach peak values around 1600 LST. This is primarily due to increase in cold pool activity at 1000 LST, reaching peak intensity between 1200-1800 LST as depicted in the Figure 6a.

Figure 10. The frequency (a, b and c) of air specific humidity drop (*Δ*q_a; gKg^{-1}) in 0.5 gKg^{-1} bins (e.g. -2 gKg^{-1}*Δ*q_a corresponds to percentage of events with air specific humidity drop between -2 to -2.5 gKg^{-1}), (d, e and f) enhancement of wind speed (*ΔWS*; ms^{-1}) in every 1 ms^{-1} bins, (g, h, i) enhancement in *SHF* (*ΔSHF*; Wm^{-2}) in every 10 Wm^{-2} bins, and (j, k, and l) enhancement in *LHF* (*ΔLHF*; Wm^{-2}) in every 20 Wm^{-2} bins due to the single cold pool events at (left) 15°N, 90°E, (middle) 12°N, 90°E and (right) 8°N, 90°E during summer (May-September). The numbers in the top and bottom panels represent the mean of atmospheric parameters.

Figure 11. Composite evolution of (a, b and c) *SHF* anomaly (Wm^{-2}) and (d, e, and f) *LHF* anomaly (Wm^{-2}) 4-hr before and after the single cold pool events at (a and d) 15°N, 90°E, (b and e) 12°N, 90°E and (c and f) 8°N, 90°E. *SHF* (black line), *SHF* estimation retaining only the enhancement of wind speed (*SHF_WS*; green line), and only the reduction of T_a (*SHF_*T_a; green line) are presented in the top panels. *LHF* (black line), *LHF* estimation retaining only the enhancement of wind speed (*LHF_WS*; green line) and only the reduction of q_a (*LHF_*q_a; green line) are presented in the bottom panels. The cyan line represents the (top panels) sum of *SHF_*T_a and *SHF_WS and* (bottom panels) sum of *LHF_*q_a and *LHF_WS.* The numbers in the top and bottom panels represent the mean value of enhancement of *SHF* (Wm^{-2}) and *LHF* (Wm^{-2}) during the cold pool, respectively.

Figure 12. The composite evolution of diurnal variability of TRMM rainfall (mm hr^{-1}) during those days with single cold pool events during (a) 0000-0600 LST, (b) 0600-1200 LST, (c) 1200-1800 LST and (d) 1800-2400 LST. The Hovmoller diagram of composite of TRMM rainfall (mm hr^{-1}) averaged over (e) a longitude band 85°E-95°E and (f) a latitude band 12°N-15°N. The black dashed arrows in the panel (e) and (f) are presented to depict the

propagating nature of rainfall. Time in LST hours. The pink circles in the panels (a) to (d) represent mooring locations at 15°N, 12°N and 8°N.

Figures with captions

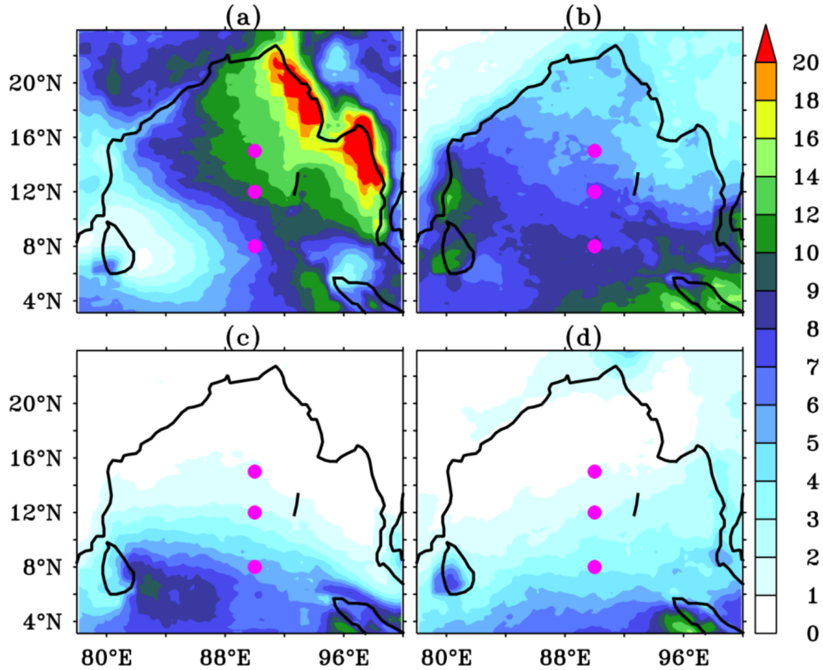

Figure 1. The seasonal average (1998-2017) of TRMM rainfall (mm day^{-1}) during (a) summer (May-September), (b) fall (October-November), (c) winter (December-February), and (d) spring (March-April) in the BoB. The RAMA mooring locations in the BoB are marked in pink circles.

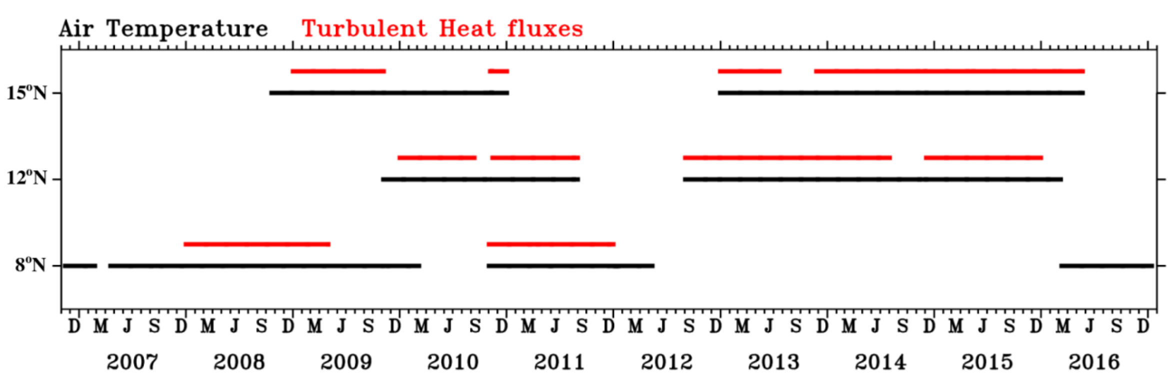

Figure 2. The availability of air temperature (black) and turbulent heat fluxes (red; *LHF* and *SHF*) from the RAMA mooring at 15°N, 90°E, 12°N, 90°E and 8°N, 90°E.

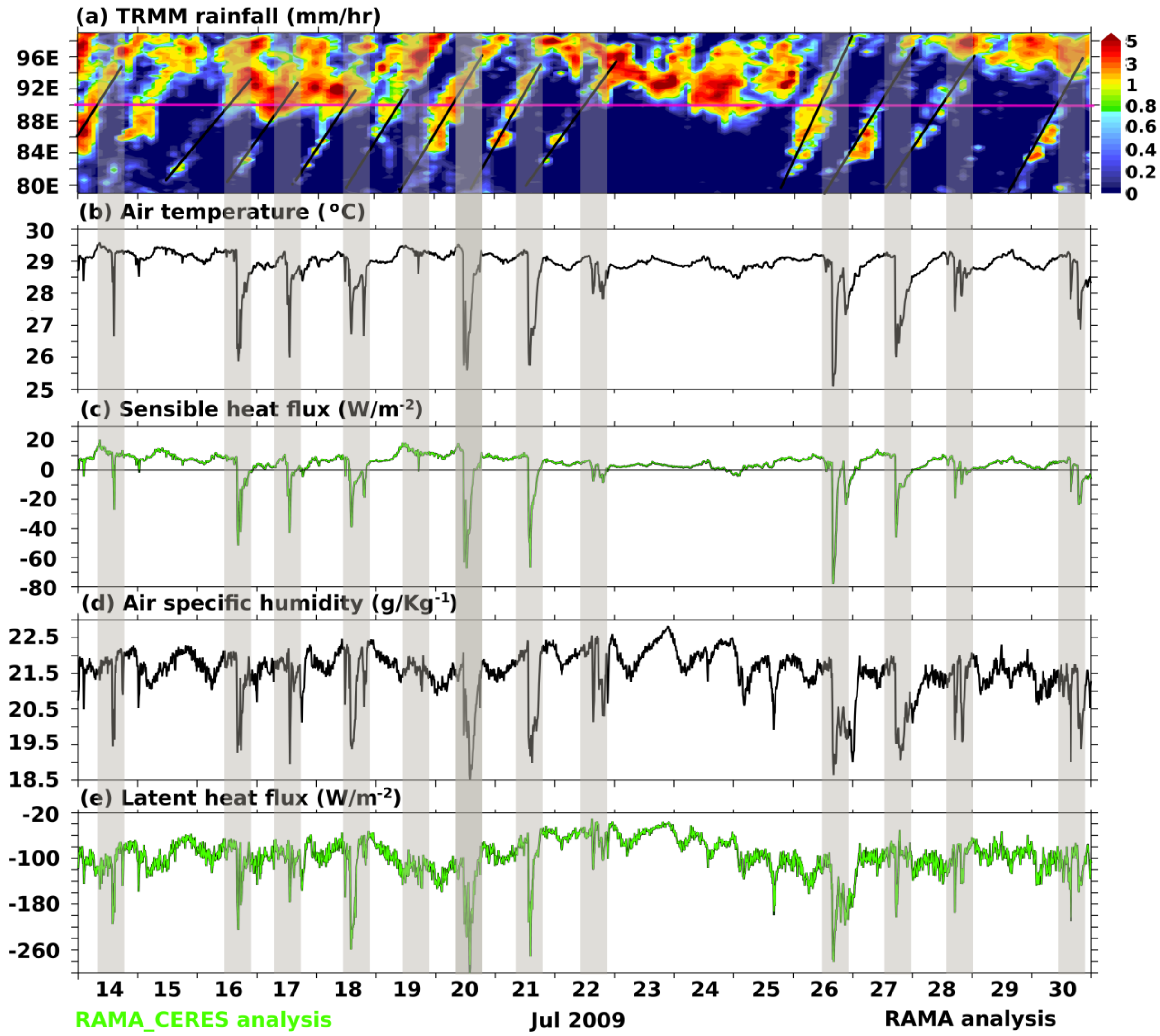

Figure 3. (a) The hovmoller diagram of TRMM rainfall (mm hr^{-1}) averaged over a latitude band 13°N-17°N. The temporal evolution of (b) air temperature (°C; T_a) (c) sensible heat flux (W m^{-2}; *SHF*), (d) air specific humidity (g Kg^{-1}; q_a) and (e) latent heat flux (W m^{-2}; *LHF*) from RAMA mooring at 15°N, 90°E during 14-30 July 2009. The tilted black lines in the panel (a) depict the offshore propagation of rainfall band. The pink horizontal line in the panel (a) represents the RAMA mooring location at 90°E. The cold pool events at the mooring locations are highlighted in the grey transparent shading. In the panels (c) and (e) the black line represents RAMA analysis and green line represents RAMA_CERES analysis.

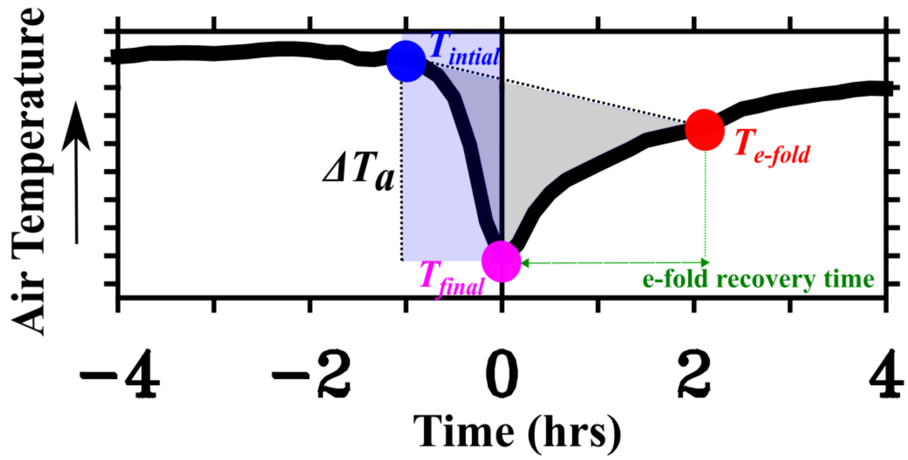

Figure 4. A schematic of a typical cold pool event based on air temperature drop and its e-folding recovery time. The cold pool active duration is defined as the period between when air temperature starts to decrease (T_{intial}) and when it reaches the minimum value (T_{final}). The difference in air temperature (ΔT_a) at T_{intial} and T_{final} is used to quantify cold pool intensity The cold pool recovery time is defined in terms of an e-folding (1/e) recovery time ($T_{e\text{-}fold}$), such as the air temperature at T_{final} (T_{a_final}) increases by 63 % of ΔT_a ($T_{a\_final}+0.63\Delta T_a$). The responses of other parameters (e.g. ΔSHF) to the cold pool event are estimated as the difference between T_{final} minus and T_{intial} values.

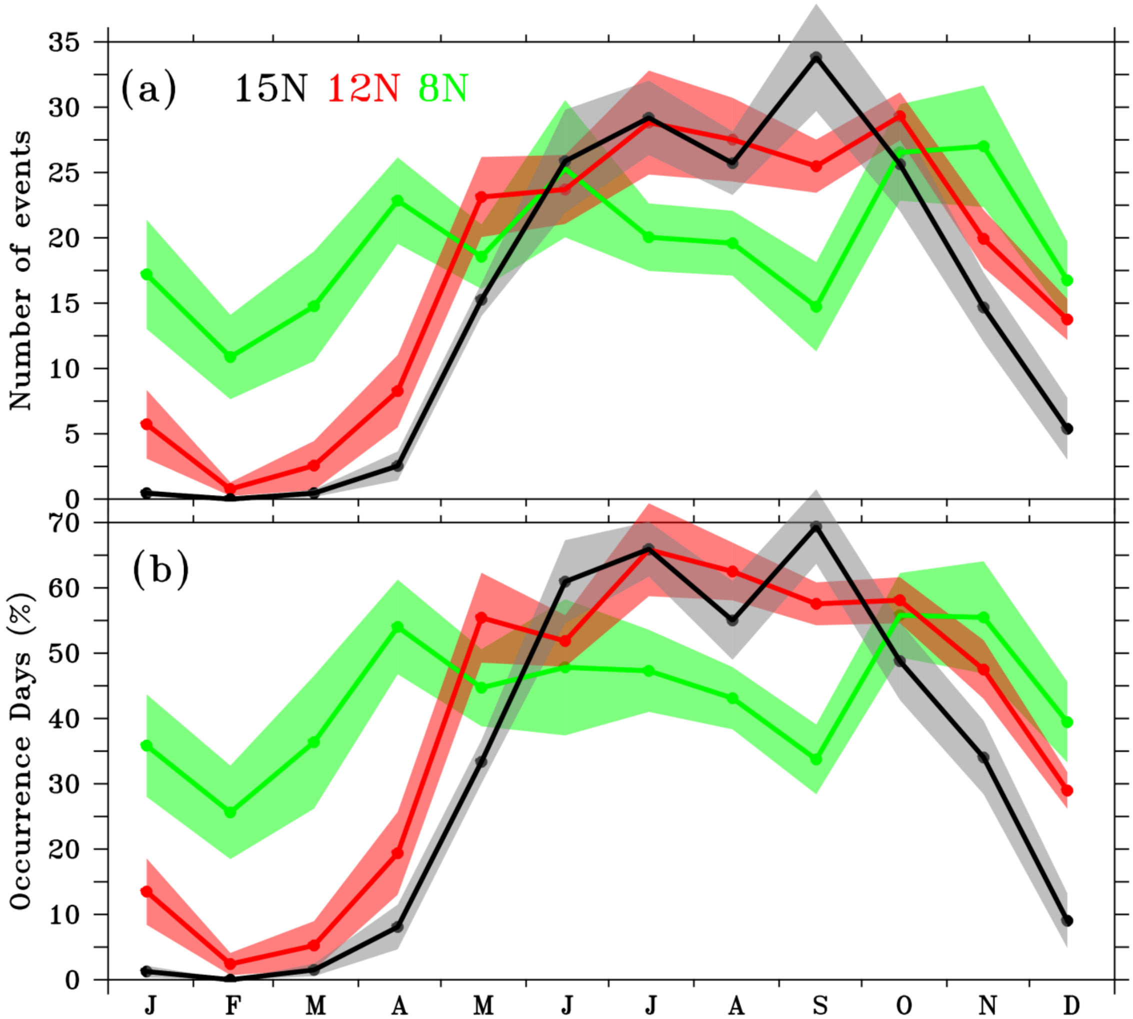

Figure 5. The monthly evolution of (a) average number of cold pool events (b) percentage of days cold pool events were reported at 15°N, 90°E, (black) 12°N, 90°E (red) and 8°N, 90°E (green) in the BoB. The seasons in this study are defined as summer (May-September), fall (October-November), winter (December-February), and spring (March-April). Shading represents estimates of one-standard error based on year-to-year deviations from the mean seasonal cycle using bootstrap methods.

.

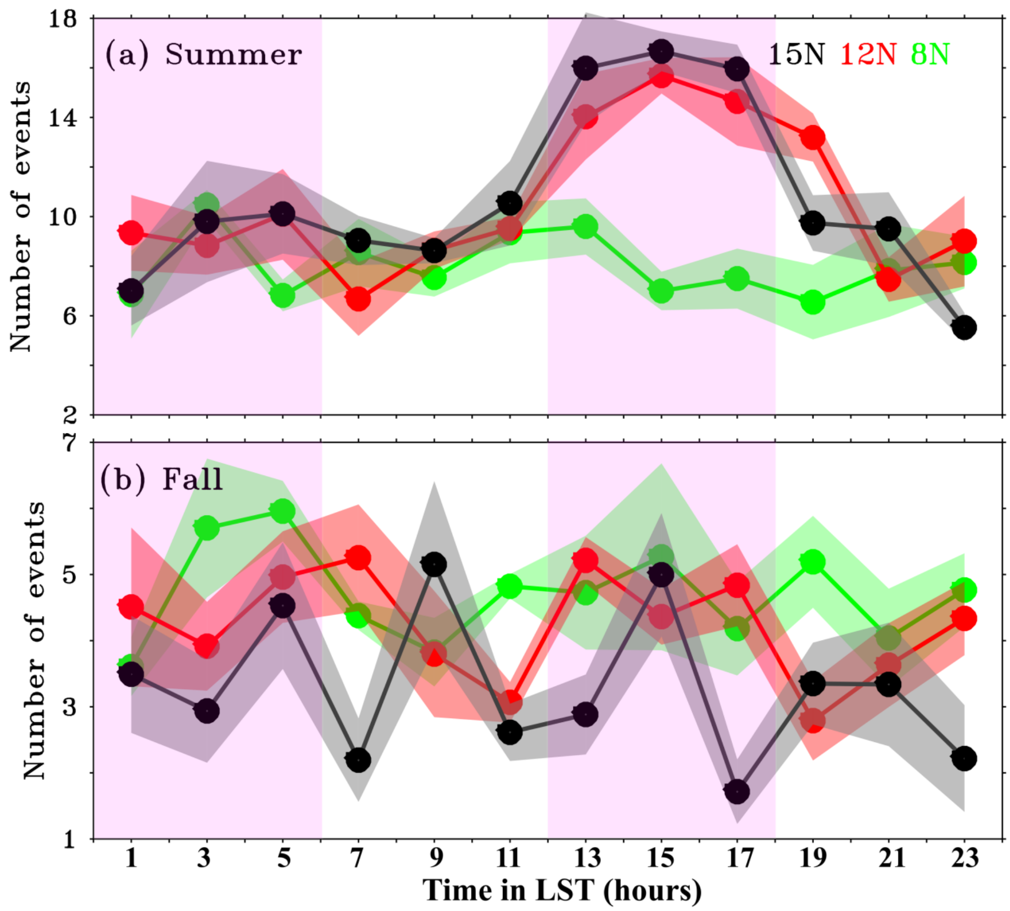

Figure 6. The average number of cold pool events observed in two-hour bins at 15°N, 90°E, (black) 12°N, 90°E (red) and 8°N, 90°E (green) in the BoB during (a) summer (May-September) and (b) fall (October-November). The pink vertical shading demarcates periods used for six-hour composites (0000-0600 LST, 0600-1200 LST, 1200-1800LST and 1800-2400LST). The 2-hourly averaged values are cantered in the middle of each two hours; for instance, the number of cold pool events corresponding to 0300 LST represents the number of events between 0200 LST and 0359 LST. Note that for the calculation we considered only those years with a minimum of 70 % data availability in a season (table-S1). Shading represents estimates of one-standard error based on year-to-year deviations from the mean seasonal cycle using bootstrap methods.

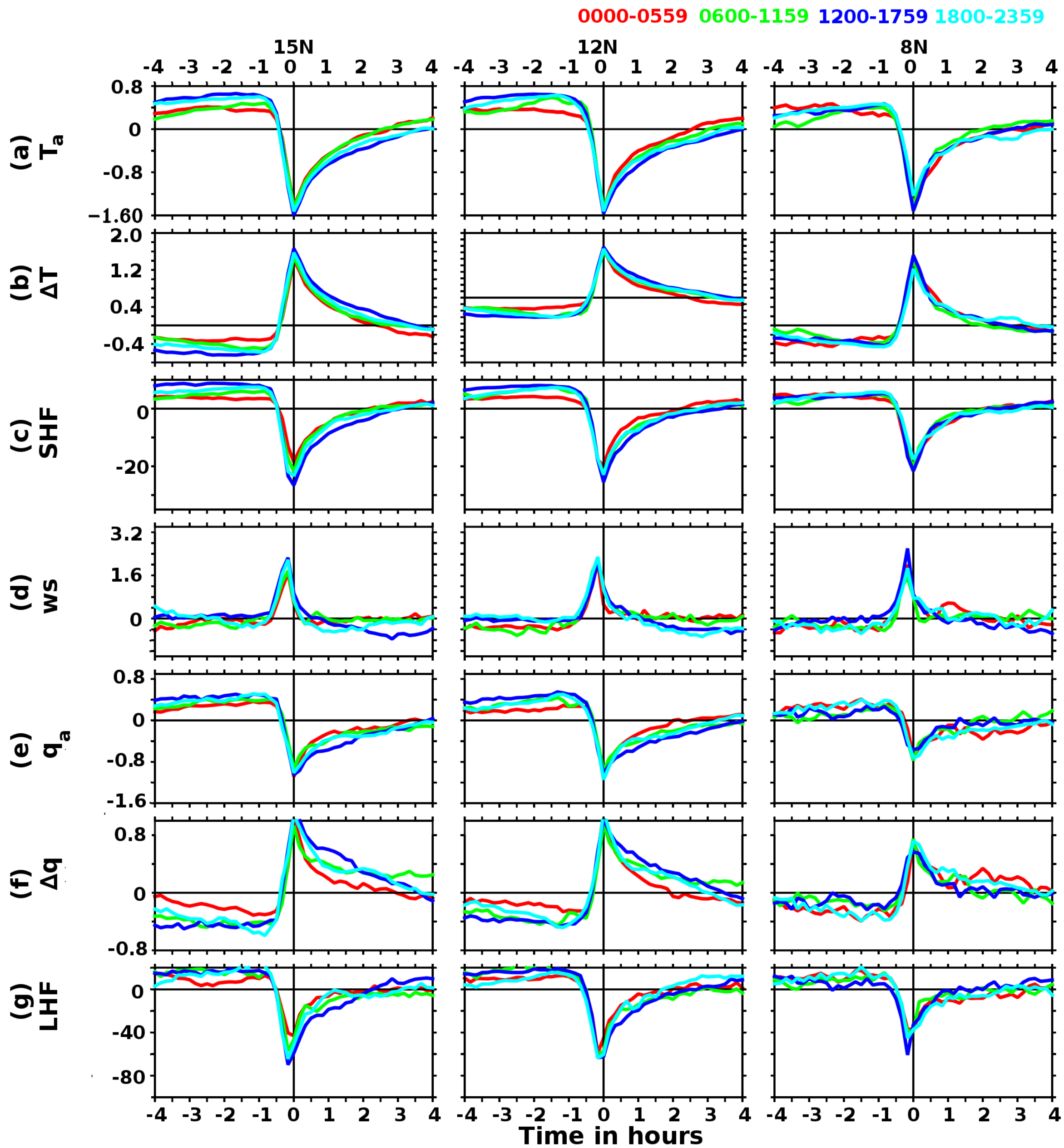

Figure 7. Composite evolution of anomaly of meteorological parameters 4-hr before and after the single cold pool events which occurred during 0000-0600 LST (red), 0600-1200 LST (green), 1200-1800 LST (blue) and 1800-2400LST (cyan) at (left) 15°N, 90°E, (middle) 12°N, 90°E and (right) 8°N, 90°E in summer (May-September). (a) air temperature (°C; T_a) (b) difference in sea surface temperature and air temperature (°C; ΔT), (c) sensible heat flux (W m^{-2}; *SHF*) (d) wind

speed (m s^{-1}), (e) air specific humidity (g Kg^{-1}; q_a), (f) difference in specific humidity between sea surface and air (g Kg^{-1}; Δq), (g) latent heat flux (W m^{-2}; *LHF*).

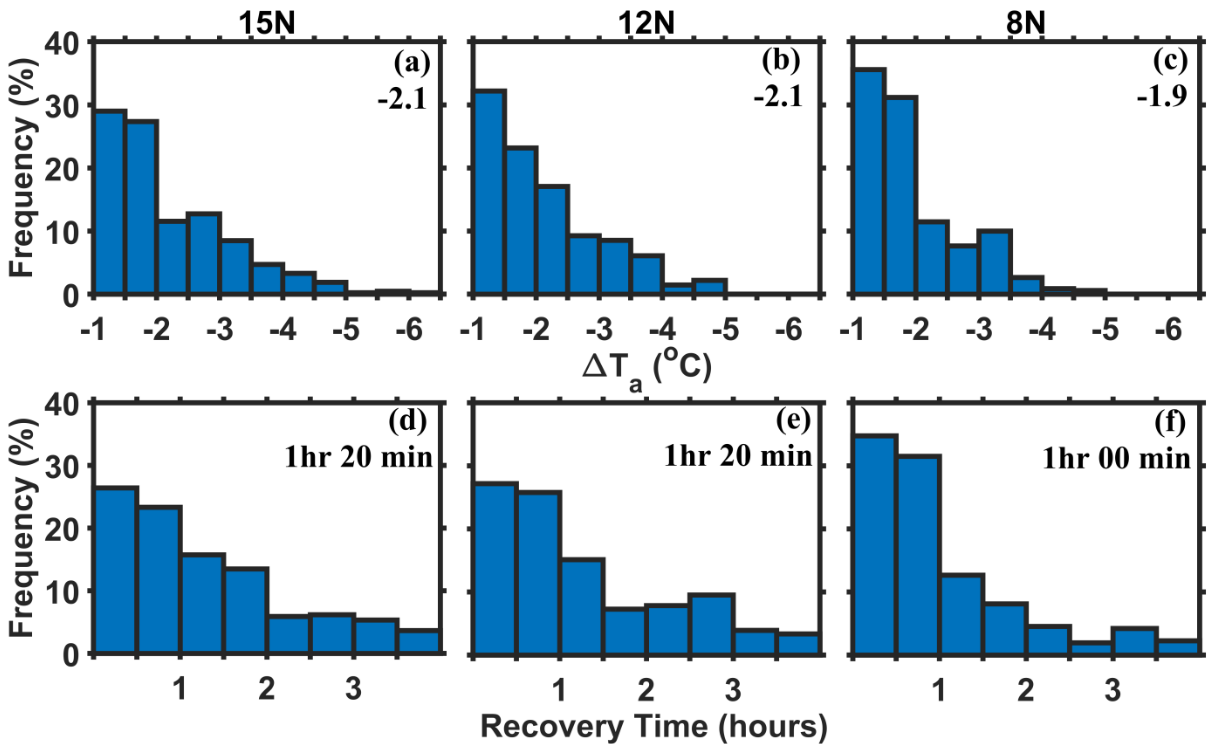

Figure 8. The frequency (a, b and c) of air temperature drop (°C; ΔT_a) in 0.5°C bins (e.g. -2°C ΔT_a corresponds to percentage of events with air temperature drop between -2 to -2.5°C) and (d, e and f) e-folding recovery time (hours) in 30 min bins (e.g. 1-hour corresponds to percentage of events with recovery time between 30-min to 1-hours) due to the single cold pool events at (left) 15°N, 90°E, (middle) 12°N, 90°E and (right) 8°N, 90°E during summer (May-September). The numbers in the top and bottom panels represent the mean of air temperature drop (°C) and e-folding recovery time (hours), respectively. Note that, we considered only those cold pool events with air temperature drop more than 1°C, hence, in the panels (a)-(c) the minimum drop restricted 1°C.

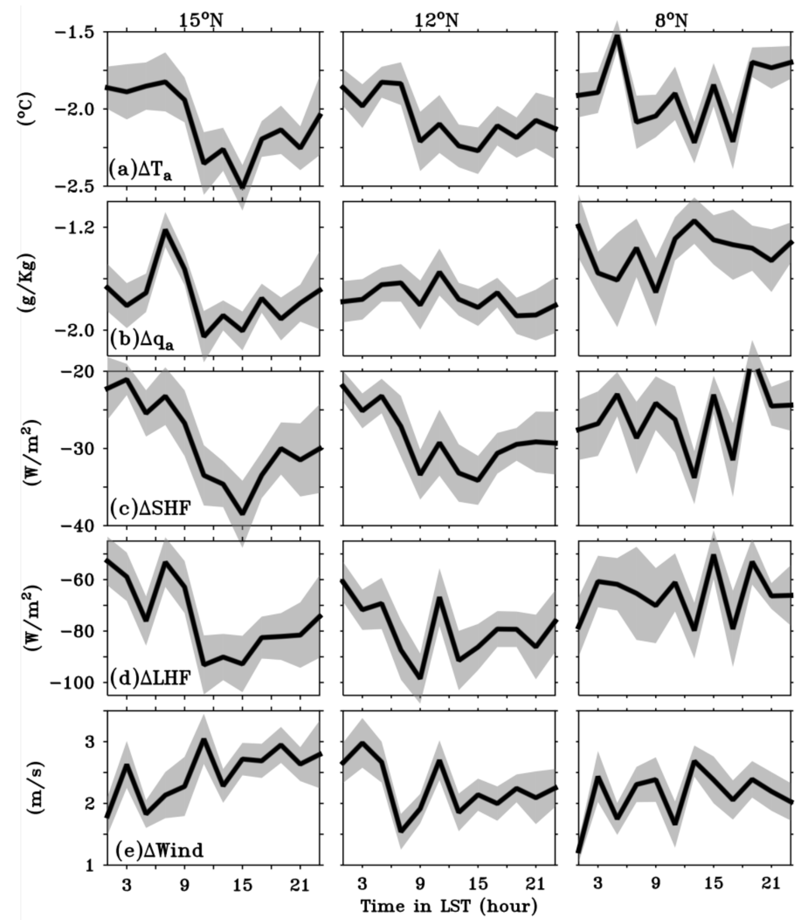

Figure 9. The diurnal variability of maximum response of surface meteorological parameters due to single cold pool events with respect to pre-cold pool conditions averaged over two-hour bins during summer (May-September). (a) reduction in air temperature (°C; ΔT_a), (b) reduction in specific humidity (g Kg^{-1}; Δq_a) (c) enhancement in sensible heat flux loss (W m^{-2}; ΔSHF) (d) enhancements in latent heat flux loss (W m^{-2}; ΔLHF), (e) enhancement in wind speed (m s^{-1}; ΔWS) at (left) 15°N, 90°E, (middle) 12°N, 90°E and (right) 8°N, 90°E. The 2-hourly averaged values are centered at the middle of each two-hour period; for instance, ΔT_a corresponding to 0300 LST represents the average value between 0200 LST and 0339 LST. Shading represents estimates of one-standard error based on year-to-year deviations from the mean seasonal cycle using bootstrap methods. Time in LST hours. Note that response of surface meteorological parameters shows a

sudden enhancement around 1000 LST and reach peak values around 1600 LST. This is primarily due to increase in cold pool activity at 1000 LST, reaching peak intensity between 1200-1800 LST as depicted in the Figure 6a.

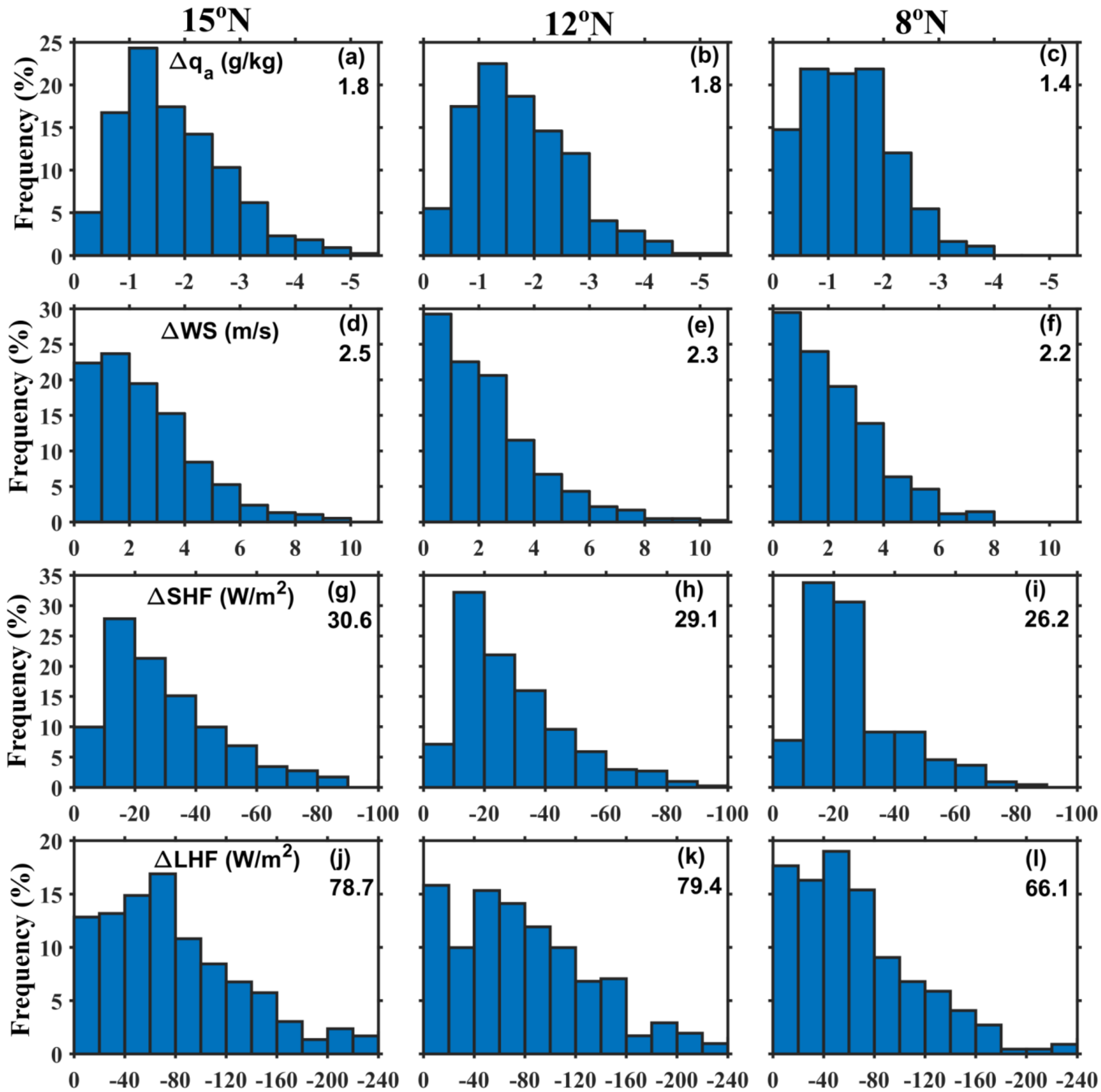

Figure 10. The frequency (a, b and c) of air specific humidity drop (Δq_a; gKg^{-1}) in 0.5 gKg^{-1} bins (e.g. -2 gKg^{-1} Δq_a corresponds to percentage of events with air specific humidity drop between -2 to -2.5 gKg^{-1}), (d, e and f) enhancement of wind speed (ΔWS; ms^{-1}) in every 1 ms^{-1} bins, (g, h and i) enhancement in *SHF* (ΔSHF; Wm^{-2}) in every 10 Wm^{-2} bins, and (j, k, and l) enhancement in *LHF* (ΔLHF; Wm^{-2}) in every 20 Wm^{-2} bins due to the single cold pool events at (left) 15°N, 90°E, (middle) 12°N, 90°E and (right) 8°N, 90°E during summer (May-September). The numbers in the top and bottom panels represent the mean of atmospheric parameters.

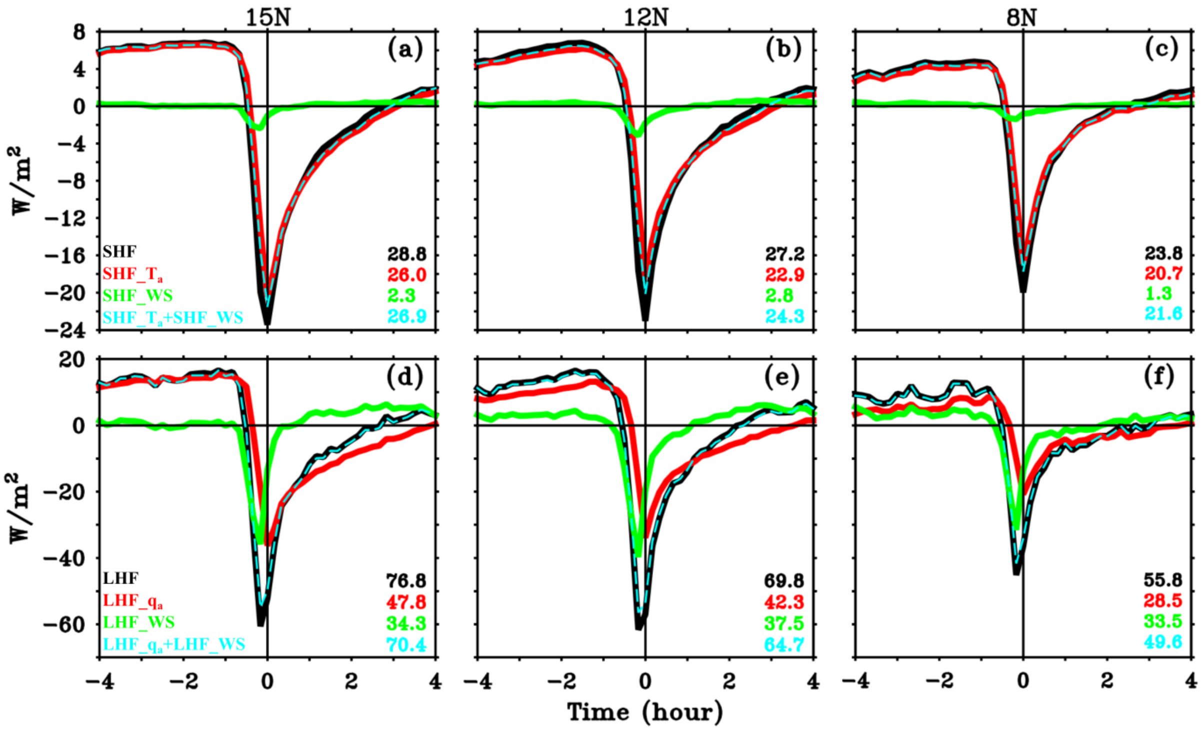

Figure 11. Composite evolution of (a, b and c) *SHF* anomaly (Wm^{-2}) and (d, e, and f) *LHF* anomaly (Wm^{-2}) 4-hr before and after the single cold pool events at (a and d) 15°N, 90°E, (b and e) 12°N, 90°E and (c and f) 8°N, 90°E. *SHF* (black line), *SHF* estimation retaining only the enhancement of wind speed (*SHF_WS*; green line), and only the reduction of T_a (*SHF_*T_a; green line) are presented in the top panels. *LHF* (black line), *LHF* estimation retaining only the enhancement of wind speed (*LHF_WS*; green line) and only the reduction of q_a (*LHF_*q_a; green line) are presented in the bottom panels. The cyan line represents the (top panels) sum of *SHF_*T_a and *SHF_WS and* (bottom panels) sum of *LHF_*q_a and *LHF_WS.* The numbers in the top and bottom panels represent the mean value of enhancement of *SHF* (Wm^{-2}) and *LHF* (Wm^{-2}) during the cold pool, respectively.

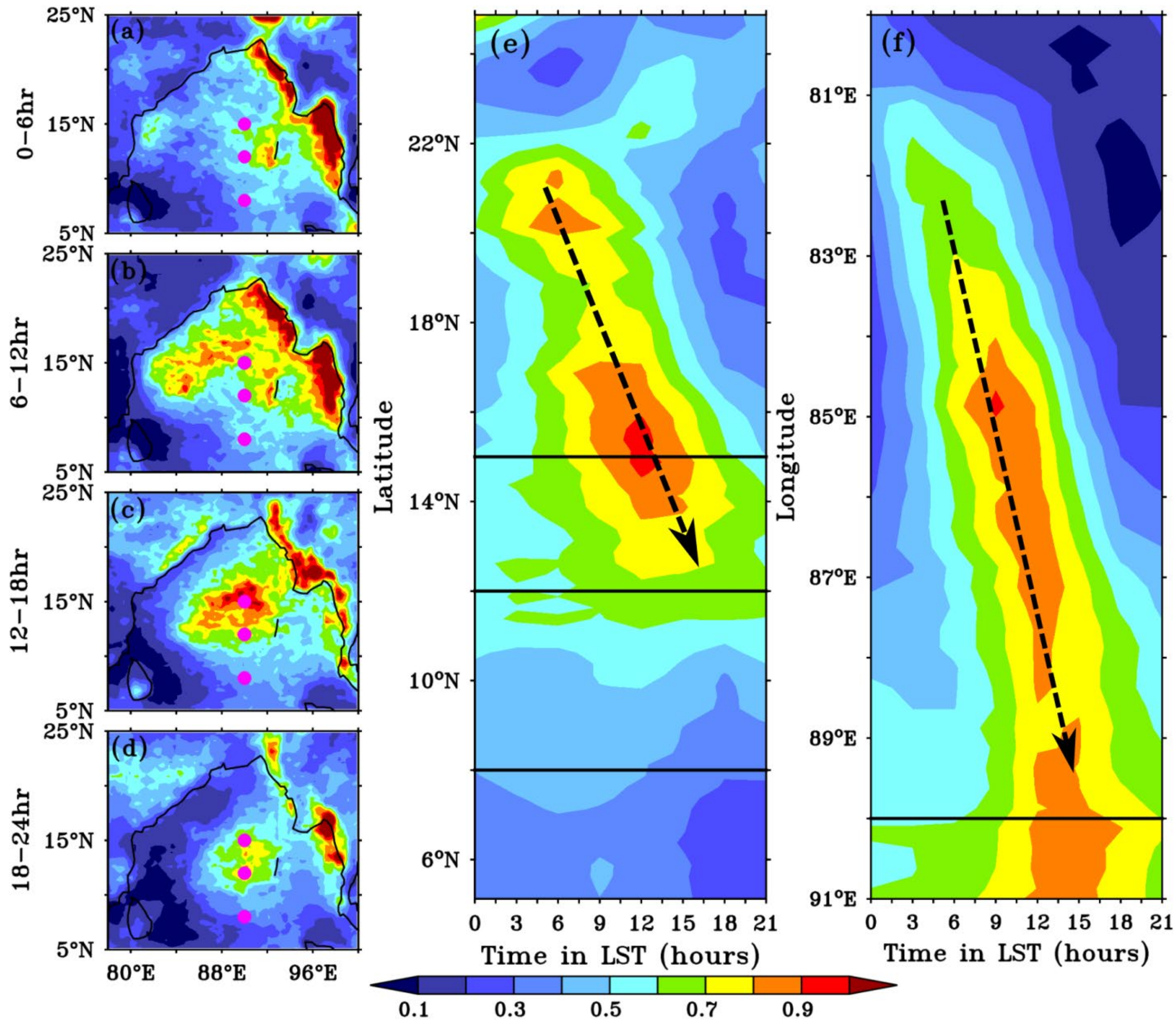

Figure 12. The composite evolution of diurnal variability of TRMM rainfall (mm hr^{-1}) during those days with single cold pool events during (a) 0000-0600 LST, (b) 0600-1200 LST, (c) 1200-1800 LST and (d) 1800-2400 LST. The Hovmoller diagram of composite of TRMM rainfall (mm hr^{-1}) averaged over (e) a longitude band 85°E-95°E and (f) a latitude band 12°N-15°N. The black dashed arrows in the panel (e) and (f) are presented to depict the propagating nature of rainfall. Time in LST hours. The pink circles in the panels (a) to (d) represent mooring locations at 15°N, 12°N and 8°N.

Tables

Coldpool events	15°N	12°N	8°N
Summer			
Total	651	634	491
Single	436 (67 %)	418 (66 %)	347 (70 %)
Double	139 (21 %)	129 (20 %)	88 (18 %)
Multiple	76 (11 %)	87 (13 %)	59 (12 %)
Fall			
Total	224	256	303
Single	164 (73%)	175 (68%)	219 (72%)
Double	40 (18%)	53 (21%)	54 (18 %)
Multiple	20 (9%)	28 (11 %)	30 (10%)

Table 1. The number of total, single, double and multiple cold pool events observed at different mooring locations (15°N, 12°N, and 8°N) in the BoB during the summer (May-September) and fall (October-December). The numbers in the brackets (rows 3-5) indicate the percentage of occurrence of each category based on the total events observed at respective mooring locations.

	15ºN				12ºN				8ºN			
Hour bin	**All**	**Single**	**Double**	**Multiple**	**All**	**Single**	**Double**	**Multiple**	**All**	**Single**	**Double**	**Multiple**
0-6	135 (20.7)	94 (21.6)	23 (16.5)	18 (23.7)	140 (22.1)	102 (24.4)	24 (18.6)	14 (16.1)	122 (24.8)	87 (25.1)	17 (19.3)	18 (32.1)
6-12	144 (22.1)	82 (18.8)	37 (26.6)	25 (32.9)	127 (20.0)	81 (19.4)	25 (19.4)	21 (24.1)	131 (26.7)	86 (24.8)	30 (34.1)	15 (26.8)
12-18	247 (37.9)	159 (36.5)	63 (45.3)	25 (32.9)	216 (34.1)	134 (32.1)	46 (35.7)	36 (41.4)	123 (25.1)	89 (25.6)	20 (22.7)	14 (25.0)
18-24	125 (19.2)	101 (23.2)	16 (11.5)	8 (10.5)	151 (23.8)	101 (24.2)	34 (26.4)	16 (18.4)	115 (23.4)	85 (24.5)	21 (23.9)	9 (16.1)

Table 2. The number of different categories of the cold pool events (all the events, single events, double events, and multiple events) is identified at different mooring locations (15°N, 12°N, and 8°N) in the BoB during summer (May-September) in 6-hour bins (0000-0600 LST, 0600-1200 LST, 1200-1800 LST, and 1800-2400 LST). The number in the bracket indicates the percentage of occurrence of cold pool event in every 6-hour bins based on the respective category of events observed at each mooring location.